Structural Studies of Wild-Type and Val120Thr Mutant *Candida boidinii* Formate Dehydrogenase

by

Mehmet Gül

A Dissertation Submitted to the
Graduate School of Sciences and Engineering
in Partial Fulfillment of the Requirements for
the Degree of

Master of Science

in

Molecular Biology and Genetics

KOÇ ÜNİVERSİTESİ

September 12, 2023

Structural Studies of Wild-Type and Val120Thr Mutant *Candida boidinii* Formate Dehydrogenase

Koç University

Graduate School of Sciences and Engineering

This is to certify that I have examined this copy of a master's thesis by

Mehmet Gül

and have found that it is complete and satisfactory in all respects,
and that any and all revisions required by the final
examining committee have been made.

Committee Members:

_____

Asst. Prof. Hasan Demirci (Advisor)

_____

Asst. Prof. Ayşe Koca Çaydaşı

_____

Assoc. Prof. Huri Dedeakayoğulları

Date: _____

To my family...

ABSTRACT

Structural Studies of Wild-Type and Val120Thr Mutant *Candida boidinii* Formate Dehydrogenase

Mehmet Gül

Master of Science in Molecular Biology and Genetics

September 12, 2023

Candida boidinii NAD^+-dependent formate dehydrogenase (*Cb*FDH) has attracted considerable interest owing to its potential in generating biofuels and various industrial chemicals from carbon dioxide (CO_2). In an endeavor to enhance its utility, this study introduces essential insights regarding the molecular structures of *Cb*FDH variants. These insights provide details that will help our understanding of the enzyme's functional mechanisms and its inherent potential for protein engineering.

Employing advanced methodologies at the Turkish Light Source *"Turkish DeLight"*, the atomic X-ray crystal structures of both the wild-type *Cb*FDH and the Val120Thr mutant were determined. These structures were obtained at different temperatures, cryogenic and ambient, thereby offering a holistic comprehension of the enzyme's dynamics under diverse environmental settings.

A key aspect of importance centers around the newly discovered hydrogen bonds within the active site of the Val120Thr mutant. The formation of these bonds between Thr120 and water molecules implies a potential enhancement of the active site's stability. Additionally, it suggests the likelihood of an improved electron transfer during the enzymatic reaction. These structural differences provide a foundation for understanding the mutant's increased effectiveness in catalyzing formate conversion—a characteristic with significant promise for industrial applications.

It is important to note that while these structural observations offer exciting prospects, further experimental data are required to validate the hypothesized mechanisms. Co-crystallization with the coenzyme and substrate has the potential to offer further insights, allowing a comprehensive understanding of the role of the identified hydrogen bonds in enhancing *Cb*FDH's capabilities.

In conclusion, the knowledge gained from the X-ray crystal structures of *Cb*FDH

in its wild-type and Val120Thr mutant forms, provides a foundation for future advancements in the field of protein engineering. As researchers delve further into the functional implications of the observed structural changes, the potential for harnessing *Cb*FDH's catalytic abilities in biotechnological applications becomes increasingly feasible. This study highlights the dynamic relationship between structural insights and practical applications, underscoring the exciting possibilities for optimizing enzymatic processes in service of a more sustainable future.

ÖZETÇE

Yabanıl Tip ve Val120Thr Mutant *Candida boidinii* Format Dehidrojenazın Yapısal Çalışmaları
Mehmet Gül
Moleküler Biyoloji ve Genetik, Yüksek Lisans
12 Eylül 2023

Candida boidinii NAD^+-bağımlı format dehidrojenaz (*Cb*FDH), karbondioksitten (CO_2) biyoyakıt ve çeşitli endüstriyel kimyasallar üretme potansiyeli nedeniyle büyük ilgi görmektedir. Bu çalışma, *Cb*FDH varyantlarının moleküler yapılarına ilişkin önemli bilgiler sunmaktadır. Bu bilgiler, enzimin işlevsel mekanizmalarını ve protein mühendisliği için potansiyelini anlamamıza yardımcı olacak ayrıntılar sunmaktadır.

Türk Işık Kaynağı *"Turkish DeLight"*'ta ileri düzey metodolojiler kullanılarak, hem yabanıl tip *Cb*FDH'nin hem de Val120Thr mutantının atomik X-ışını kristal yapıları belirlenmiştir. Bu yapılar, kriyojenik ve ortam sıcaklığı gibi farklı sıcaklıklarda elde edilmiş, böylece enzimin farklı çevresel koşullar altındaki dinamiklerinin bütünsel bir şekilde anlaşılması sağlanmıştır.

Val120Thr mutantının aktif bölgesinde yeni keşfedilen hidrojen bağları önemli bir noktadır. Thr120 ve su molekülleri arasında bu bağların oluşması, aktif bölgenin stabilitesinde potansiyel bir artış anlamına gelmektedir. Ayrıca, enzimatik reaksiyon sırasında gelişmiş bir elektron transferi olasılığını da ortaya koymaktadır. Bu yapısal farklılıklar, mutantın format dönüşümünü katalize etmedeki artan etkinliğini anlamak için bir temel sağlar, bu özellik endüstriyel uygulamalar için önemli bir umut vaat etmektedir.

Bu yapısal gözlemler heyecan verici beklentiler sunarken, varsayılan mekanizmaları doğrulamak için daha fazla deneysel veriye ihtiyaç olduğunu belirtmek önemlidir. Koenzim ve substrat ile birlikte kristalizasyon, tanımlanan hidrojen bağlarının *Cb*FDH'in yeteneklerini geliştirmedeki rolünün kapsamlı bir şekilde anlaşılmasına olanak tanıyarak daha fazla bilgi sunma potansiyeline sahiptir.

Sonuç olarak, *Cb*FDH'nin yabanıl tip ve Val120Thr mutant formlarının X-ışını kristal yapılarından elde edilen bilgiler, protein mühendisliği alanında gelecekteki il-

erlemeler için bir temel oluşturmaktadır. Araştırmacılar gözlemlenen yapısal değişikliklerin işlevsel sonuçlarını daha fazla araştırdıkça, biyoteknolojik uygulamalarda *Cb*FDH'nin katalitik yeteneklerinden yararlanma potansiyeli giderek daha mümkün hale gelmektedir. Bu çalışma, daha sürdürülebilir bir geleceğin hizmetinde enzimatik süreçleri optimize etmek için heyecan verici olasılıkların altını çizerek yapısal iccgörüler ve pratik uygulamalar arasındaki dinamik ilişkiyi vurgulamaktadır.

ACKNOWLEDGMENTS

I am deeply grateful to Asst. Prof. Hasan Demirci, whose support and mentorship have been influential in my academic growth. He has not only been my advisor but also a source of inspiration, encouraging me to strive for excellence and to persevere through the challenges of research.

I would also like to extend my appreciation to Assoc. Prof. Huri Dedeakayoğulları, who has played a crucial role in my academic journey. Her guidance and expertise, as well as her friendship, have been invaluable in my personal and academic life.

Additionally, I extend my heartfelt thanks to the member of my thesis committee, Asst. Prof. Ayşe Koca Çaydaşı, for her time in evaluating my research.

I would also like to extend my heartfelt gratitude to the members of KUYBIIG-M for their friendship, collaboration, and enriching scientific discussions. I would especially like to thank my friends Alaleh Shafiei, Barış Çakılkaya, Betül Ertem, Bilge Tosun, Büşra Yüksel, Cahine Kulakman, İlkin Yapıcı, Merve Yılmaz, Murat Kaan Şentürk, Ömür Güven, and Serra Tavlı for being such great friends and always being there for me.

Words cannot adequately express my gratitude to my beloved family, who have been my unwavering source of support and love throughout my academic journey. I extend my deepest thanks to my mother, Hayriye, my father, Ahmet, and my little brother, Berkay. Your encouragement, sacrifices, and unending love have been the driving force behind my accomplishments. This thesis would not have materialized without your constant belief in me.

TABLE OF CONTENTS

LIST OF TABLES

LIST OF FIGURES

ABBREVIATIONS

ADP	Adenosine Diphosphate
Ala	Alanine
Arg	Arginine
Asn	Asparagine
Asp	Aspartic Acid
ATP	Adenosine Triphosphate
*Cb*FDH	*Candida boidinii* formate dehydrogenase
CH_4	Methane
CO	Carbon Monoxide
CO_2	Carbon Dioxide
Cys	Cysteine
ddH_2O	Deionized distilled water
DFFC	Direct Formate Fuel Cell
DLFC	Direct Liquid Fuel Cell
DNA	Deoxyribonucleic Acid
FDH	Formate dehydrogenase
Gln	Glutamine
Glu	Glutamic Acid
h	Hour
H_2	Hydrogen
His	Histidine
Ile	Isoleucine
IPTG	Isopropyl β-D-1-thiogalactopyranoside
K	Kelvin
kDa	Kilodalton

k_{cat}	Turnover Number
K_M	Michaelis Constant
kV	Kilovolt
L	Liter
LB	Luria-Bertani
mA	Milliampere
MD	Molecular Dynamics
MES	2-(N-morpholino)ethanesulfonic Acid
Met	Methionine
min	Minute
ml	Milliliter
mm	Millimeter
mM	Millimolar
MME	N-methyl Methionine
mV	Millivolt
NAD	Nicotinamide Adenine Dinucleotide
NADH	Nicotinamide Adenine Dinucleotide Hydrogen
NADP	Nicotinamide Adenine Dinucleotide Phosphate
Ni-NTA	Nickel-Nitrilotriacetic Acid
PCR	Polymerase Chain Reaction
PDB	Protein Data Bank
PEG	Polyethylene Glycol
Phe	Phenylalanine
*Pse*FDH	*Pseudomonas sp.* 101 FDH
QM/MM	Quantum Mechanics/Molecular Mechanics
RMSD	Root Mean Square Deviation
rpm	Revolutions per Minute
SDS	Sodium Dodecylsulfate
SDS-PAGE	SDS-Polyacrylamide Gel Electrophoresis

sec	Second
Ser	Serine
sp.	Species
Thr	Threonine
TLS	Translation/Libration/Screw
UV	Ultraviolet
V	Volt
Val	Valine
W	Watt
Wt	Wild-type
XRD	X-ray Diffractometer
Å	Ångström
µl	Microliter

Chapter 1

INTRODUCTION

1.1 Formate

Formate, the anionic form of formic acid, plays a pivotal role in the metabolism of both microorganisms and mammals. Its name originates from its initial isolation from ants, deriving from the Latin term *"formica"* (Brosnan and Brosnan, 2020). Formic acid serves as a significant energy source for microorganisms due to its redox potential of -420 mV (Sawers et al., 2004, Pinske and Sawers, 2016). Furthermore, it is an integral component of the *"one-carbon metabolism"* in these organisms (Ducker and Rabinowitz, 2017, Gopalakrishnan et al., 2019).

Within human metabolism, it is regenerated via both folate-dependent and folate-independent pathways, serving as an intermediary metabolite (Pietzke et al., 2020). In energy production, formate is commonly transformed through different enzymatic pathways or eliminated by conversion to CO_2 and hydrogen (Alissandratos et al., 2013, Gopalakrishnan et al., 2019).

Formate found in mammalian blood and other bodily fluids functions as an indirect marker for identifying conditions such as methanol poisoning or vitamin B12 deficiency. The metabolic breakdown of methanol results in the formation of formate via formaldehyde, and elevated concentrations of formate in bodily fluids indicate methanol intoxication (Hovda et al., 2021). Likewise, a marked increase in formate levels is associated with vitamin B12 deficiency (Lamarre et al., 2013).

1.2 Formate in Biotechnology and Industry

Formate stands as a crucial one-carbon organic compound within carbon and energy metabolism. It operates as a versatile metabolite, engaging in fixation through diverse enzymes and pathways across a range of organisms and biological contexts. The conversion from carbon dioxide to formate is achieved via multiple mechanisms, such as enzymatic reduction, CO_2 hydrogenation, natural gas oxidation, photoreduction, and electroreduction (Maia et al., 2021, Wang et al., 2020, Lehn and Ziessel, 1990, Han et al., 2022). Beyond its significance in the biological realm, it holds substantial utility as an intermediary in biotechnological and industrial sectors, supporting the synthesis of chemicals, biofuels, and carbon reduction/sequestration processes. Notably, formate offers a secure and environmentally friendly option for energy storage, presenting advantages over hydrogen (Grubel et al., 2020, Vo et al., 2015, Song et al., 2017). Apart from its intermediary role in diverse physicochemical and biological activities, the conversion of CO_2 to formate holds particular significance in the context of CO_2 reduction and sequestration studies, owing to the environmental importance of CO_2 as a greenhouse gas (Bar-Even, 2016).

Formate, in the form of formic acid, serves as an energy storage medium in fuel cells. Direct liquid-feed fuel cells (DLFCs) are systems that generate electricity from liquid fuels without converting them into hydrogen (Kumar et al., 2021). Among DLFCs, direct formic acid fuel cells (DFFCs) (Figure 1.1) utilize the stored biochemical energy within formic acid's bonds to produce electricity with a theoretical electrical potential of 1.48 V (Fang and Chen, 2021). This technology holds significant promise for renewable energy production, owing to its high potential and easy transportability (An and Chen, 2016). DFFCs are more environmentally friendly, less susceptible to carbon monoxide (CO) poisoning on noble metal catalysts like platinum and palladium and exhibit reduced fuel crossover compared to other DLFC types that use methanol, ascorbic acid, and similar substances (Hasan, 2023).

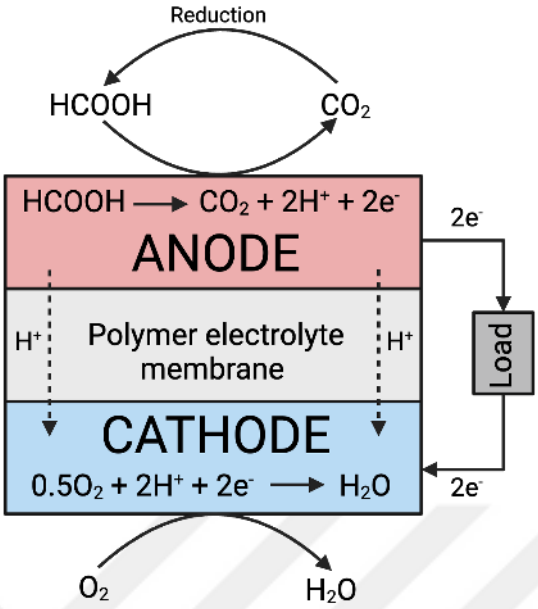

Figure 1.1: A schematic of a direct formic acid (HCOOH) fuel cell.

Formate's significance extends beyond its role in DFFCs as it is a vital precursor in biotechnological applications, including biofuel synthesis. In the biomethanation process, formate undergoes a series of transformations. Initially, it is converted into CO_2 and H_2. Subsequently, the generated CO_2 is hydrogenated to produce methane (CH_4). This sequence plays a crucial role in biofuel production strategies (Braga Nan et al., 2020).

The formate dehydrogenase enzyme (FDH) efficiently drives the reverse reaction (from carbon dioxide to formate) when formate concentrations are low (Alissandratos et al., 2013). This limitation, however, can be addressed through various strategies. For example, formate can be separated from the reaction as it is produced (Hu and Adeyiga, 1997). Alternatively, enzyme activity can be manipulated by peripheral enzymes through coenzyme regulation, pathway engineering, or allosteric regulation (Punekar, 2018, Dasgupta et al., 2020, Fastrez, 2010). Overcoming this limitation would be extremely useful due to the wide-ranging applications of formate involving microorganisms. For instance, formate serves as a valuable microbial feedstock, providing both carbon and energy. Moreover, it acts as a precursor for the production of various chemicals in the chemical industry. While many chemical reactions are sensitive to substrate purity and concentration, enzymes,

including FDH, display remarkable adaptability by catalyzing its reaction across varying levels of purity and concentration (Aledo and Medina, 2019, Ottone et al., 2021). This flexibility makes it suitable for different conditions, including anaerobic or aerobic environments, and even extreme settings like methanogenic environments or high temperatures. These beneficial features position FDH as an excellent candidate for integrating formate into biological systems through formate assimilation in biotechnology.

1.3 Nicotinamide Adenine Dinucleotide

Nicotinamide adenine dinucleotide (NAD) is a molecule comprising two nucleotides interconnected by their phosphate groups. Within this structure, one nucleotide contains a nicotinamide, whereas the other holds an adenine nucleobase. NAD exists in two main forms: oxidized (NAD^+) and reduced (NADH) (Figure 1.2). It serves as a crucial coenzyme in electron transfer during redox reactions. In these reactions, NAD^+ acts as an oxidizing agent, undergoing reduction as it accepts electrons, whereas NADH functions as a reducing agent, donating electrons and undergoing oxidation (Griffiths et al., 2020).

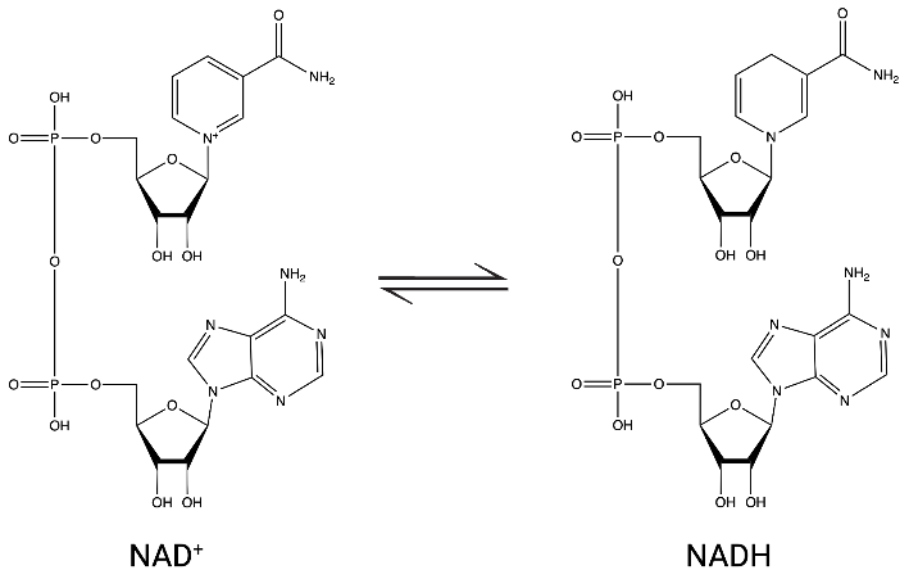

Figure 1.2: Two forms of nicotinamide adenine dinucleotide: oxidized (left) and reduced (right).

NAD plays a versatile role, serving as a substrate for various enzymes such as DNA ligase, sirtuins, and ADP-ribosylation enzymes. In post-translational protein modifications, NAD assumes the role of a substrate for enzymes responsible for the addition or removal of various chemical groups. This intricate involvement underscores the multifunctional nature of NAD in orchestrating cellular activities beyond its renowned electron transport role (Lin, 2007).

Within the context of redox reactions, while a proton is removed from another substrate, the proton within the surrounding solution is oxidized, leading to the release of NADH through its transfer to the nicotinamide ring of NAD^+. This intricate process involves the hydride electron pair transfer. One electron is directed towards the positively charged nitrogen atom of the nicotinamide ring, while the other electron is directed to the C4 carbon atom of the same ring. However, due to the reversible nature of this reaction, NAD^+ proves itself as a versatile intracellular intermediate metabolite for both reduction and oxidation processes (Griffiths et al., 2020).

While NAD primarily functions as a significant electron carrier within cellular metabolism, its significance extends to diverse processes within the cell. Beyond its role as an intracellular oxidizer in metabolic processes, NAD^+ also functions as a signal molecule. It is transported between tissues and organs such as neurons, the large intestine, brain, cardiac tissues, and urinary bladder (Breen et al., 2006, Mutafova-Yambolieva et al., 2007, Koch-Nolte et al., 2011, Durnin et al., 2012, Tannous et al., 2021)

Moreover, the disparity in UV-absorption peaks at 259 nm and 339 nm is exploited for spectroscopic identification of NAD^+ and NADH, respectively, as well as for enzyme kinetic investigations (Dawson, 1986). This distinctive feature underscores its utility in probing the dynamics of NAD^+ and NADH in various biochemical contexts.

1.4 Formate Dehydrogenase

Formate dehydrogenase (FDH) is an enzyme ubiquitous in both prokaryotic and eukaryotic organisms. Functioning as an oxidoreductase, it facilitates the reversible oxidation of formate to carbon dioxide, utilizing an electron carrier molecule. This electron carrier molecule is contingent upon the specific organism and prevailing reaction conditions, whether aerobic or anaerobic. The electron carrier molecule can be a coenzyme like NAD^+, $NADP^+$, and ferrodoxin, or a cofactor such as tungsten, molybdenum, and flavin (Ljungdahl, 1980; Fauque and Barton, 2012).

Formate dehydrogenase (FDH) is categorized into distinct groups based on the electron carrier molecule it uses. The variant of FDH that utilizes tungsten, molybdenum, or heme as its electron carrier is referred to as metal-dependent formate dehydrogenase (Fauque and Barton, 2012). This nomenclature is due to the presence of an oxidized metal within the enzyme's active site, accepting electrons from formate. Metal-dependent formate dehydrogenases are primarily found in anaerobic bacteria. Despite their facile expression in bacterial systems, these metal-dependent enzymes pose challenges in laboratory settings due to their strict requirement for anaerobic conditions.

1.4.1 NAD^+-dependent Formate Dehydrogenase

An additional category within the formate dehydrogenase family comprises the NAD^+-dependent formate dehydrogenase, where NAD^+, an organic oxidizing molecule, functions as a coenzyme for formate reduction (Niks and Hille, 2018). Extensive research has been conducted to investigate the structural and functional properties of these enzymes, with a particular focus on CO_2 reduction and its economic viability (Jayathilake et al., 2019, Ferry, 1990, Miller et al., 2019). Among the inhibitors targeting the FDH enzyme, azide and cyanide emerge as covalent inhibitors (Figure 1.3). However, their use in research is limited due to their substantial toxicity concerns (Ohyama and Yamazaki, 1975).

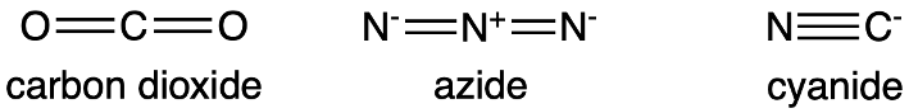

Figure 1.3: Chemical structures of carbon dioxide and FDH inhibitors azide and cyanide.

The conversion of formate to CO_2 with the help of NAD^+ (Figure 1.4) occurs within the active site of the enzyme, predominantly without the participation of cofactors (Torres et al., 1999). NAD^+-dependent FDH is especially well-suited for use in aerobic conditions, as it does not require the use of costly cofactors. Its remarkable efficiency makes it an ideal candidate for the generation of essential chemicals and for facilitating CO_2 fixation. Moreover, its applicability extends to biomedical applications, including the precise measurement of formate levels in bodily fluids. The enzyme's significance has prompted extensive research, encompassing both enzymatic and structural analyses, as well as efforts to enhance its activity through mutational studies.

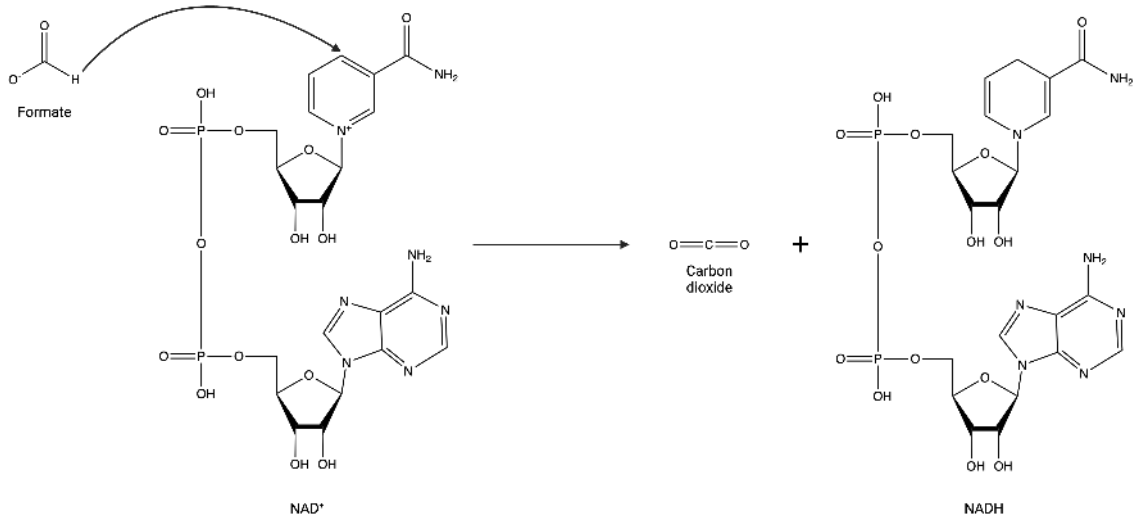

Figure 1.4: The forward reaction catalyzed by NAD^+-dependent formate dehydrogenase. The hydride group is transferred from formate ion, being oxidized to carbon dioxide, to NAD^+, reducing it to NADH.

NAD^+-dependent formate dehydrogenase stands as a central enzyme within the one-carbon metabolism, playing a crucial role in organisms like aerobic bacteria and

yeast. It belongs to the protein family of 2-hydroxy acid dehydrogenases (Nielsen et al., 2019). Functioning by using an NAD molecule for electron transfer, NAD^+-dependent formate dehydrogenase carries out its catalytic role (Torres et al., 1999).

The enzyme's active site prominently features eight conserved amino acids, including basic ones like Arg and His that form a binding site for formate or CO_2. Additionally, polar amino acids such as Asp, Thr, Gln, and Ser contribute to NAD^+/NADH binding, while Ile serves as a hydrophobic counterpart. Notably, the polar amino acids Thr, Asp, and His form a hydrogen bond network that traps NAD^+ through interactions with the hydrogens of the amide group and the carbonyl oxygen. This NAD^+ trapping is considered the initial step in the reaction mechanism. Subsequently, formate binds to the positively charged amino acids Arg and His, leading to the oxidation of formate during NAD^+ reduction (Tishkov and Popov, 2004).

Site-directed mutagenesis studies and structural analyses further confirm the significance of the His332-Gln313 pair and Arg284 in substrate binding and catalytic activity, respectively (Tishkov et al., 1996). This reaction relies on the electrostatic influences of these residues, with the reversible process being substrate-concentration-dependent due to the potential affinity of both substrate and product in NAD^+-dependent FDH (Castillo et al., 2008, Sato and Amao, 2020).

In molecular dynamics (MD) simulations, prior studies have indicated that the conserved residues (Arg284, Asn146, Ile122) maintain a suitable conformation for facilitating hydride transfer. This is achieved by bringing the formate close to the C4N group of the nicotinamide ring of NAD^+, aided by electrostatic interactions. Simultaneously, evidence has been presented to establish that Thr, Asp, His, and Ser residues, along with NAD^+, sustain this specific conformation by interacting with the active site in a trans conformation of NAD^+ (Torres et al., 1999).

Metal-independent FDHs, including NAD^+-dependent FDH, exhibit specificity towards NAD^+/NADH binding and do not naturally accommodate NADP. Moreover, among NAD^+-dependent enzymes, there is a distinct tendency for formate oxidation that surpasses the tendency for CO_2 reduction. The enzyme orchestrates hydride transfer from formate to NAD^+ with strategic positioning during the tran-

sition state. This positioning promotes effective hydride transfer and advances the progress in the forward direction (Nielsen et al., 2019).

Quantum mechanics/molecular mechanics (QM/MM) studies have validated these findings by revealing that the enzyme strategically positions formate and NAD^+ closely in the transition state. This positioning creates a suitable structure for hydride transfer, supporting the reaction in the desired direction. The same study also reported that the presence of water within the active site may perturb this transition state, slowing down the reaction. This underscores the importance of hydrophobic amino acids like Ile in the active site, maintaining the integrity of the transition state and promoting the reaction by mitigating the presence of water (Castillo et al., 2008).

1.4.2 Candida boidinii NAD$^+$-dependent Formate Dehydrogenase

Candida boidinii, a yeast strain with significant industrial uses in areas, such as methanol synthesis, biofuel production, and recombinant protein expression, expresses the NAD^+-dependent FDH (*Cb*FDH). This enzyme exists as a homodimer with a molecular weight of 84 kDa (Castillo et al., 2008)

*Cb*FDH employs a conserved mechanism for oxidizing formate by reducing NAD^+. Studies by Labrou and Rigden highlight the roles of Val123 and Ile175 in creating hydrophobic pockets that facilitate catalysis, paralleling other NAD^+-dependent FDHs (Labrou and Rigden, 2001). In parallel, Arg258 and Asn119 oversee the hydride transfer and formate binding, ensuring proper conformation and charge equilibrium. Furthermore, His311-Gln287 replaces the conventional His-Glu relay system. These residues, influenced by their electrostatic properties, guide formate interaction, directing *Cb*FDH's intricate kinetics (Labrou and Rigden, 2001).

Like other NAD^+-dependent FDH enzymes, *Cb*FDH typically favors a specific direction. However, a study on the reverse reaction, involving the conversion of CO_2 to formate, revealed a direct correlation between the production of formate and rising CO_2 concentration. This phenomenon finds its rationale in the residue composition -Asn119, Ile175, and Arg258- key to formate binding. Importantly,

these sites coincide with the sites of CO_2 attachment, thus enabling the feasibility of the reverse reaction (Sato and Amao, 2020).

The significance of *Cb*FDH goes beyond pharmaceutical applications. Its capacity for carbon reduction, with its environmentally friendly potential, enhances its value. This is especially impactful if the enzymatic turnover rate surpasses the chemical alternatives (Nielsen et al., 2019). Considering its key roles in industry and environmental efforts, protein engineering studies with the aim of increasing *Cb*FDH activity and stability, along with a comprehensive understanding of its molecular dynamics have gained considerable significance (Castillo et al., 2008)

1.5 Formate Dehydrogenase in Biotechnology and Industry

The versatility of NAD^+-dependent formate dehydrogenase encompasses various metabolic engineering applications. By manipulating cofactor/coenzyme availability, a critical rate-limiting factor, the enzyme holds potential for enhancing system efficiency. This goes beyond simple assistance for rate-limiting reaction stages and extends to fortifying fermentation by functioning as an oxidizing agent. Notably, NADH is crucial for anaerobic cell growth (Berríos-Rivera et al., 2002).

In a study, NAD^+-dependent FDH derived from *Candida boidinii* was introduced into fermentation processes to address the challenge of formate accumulation, a significant issue in succinic acid production. This application led to the elimination of formate by-products during succinic acid synthesis and concurrently increased the NADH availability (Balzer et al., 2013). Moreover, the upregulation of *Cb*FDH in *Escherichia coli* resulted in elevated NADH levels and enhanced cell density, confirming the direct impact of NADH availability on cell proliferation (Berríos-Rivera et al., 2002).

Similarly, researchers observed that *Saccharomyces cerevisiae* strains, enriched in FDH expression through adaptive laboratory evolution, displayed heightened tolerance against formate and acetate, crucial factors in bioethanol production. Notably, this study showed that the role of FDH extended beyond its conventional function of converting excessive formate to CO_2. It enhanced cellular vitality by converting

formate into acetate and ATP through CO_2 reduction, particularly when formate was absent (Du et al., 2022).

In addition to its role in producing carbon-neutral energy, such as biomass generation, FDH demonstrates environmental friendliness through CO_2 reduction. In a recent study, the CO_2 reduction mechanism of *Cb*FDH was harnessed using an artificial cofactor, methyl viologen radical cation (Jayathilake et al., 2019). Another relevant application involves the use of NAD^+-dependent FDH to regenerate NADH electrochemically for reducing CO_2 within cathodic cells. This study demonstrated that immobilizing NAD^+-dependent FDH onto electrospun polystyrene nanofibers led to improved long-term stability and reusability (Barin et al., 2018).

FDH plays a vital role in synthesizing chemicals and amino acids like methanol, succinic acid, L-alanine, and L-serine through in vivo systems. It transforms CO_2 into formate, serving as a liquid one-carbon intermediate metabolite. It is anticipated that incorporating formate assimilation pathways via FDH overexpression in different systems, like *E. coli*, will become a common approach for efficient production of various valuable chemicals (Calzadiaz-Ramirez and Meyer, 2022).

As discussed earlier, *Cb*FDH demonstrates preference for CO_2 reduction due to its interaction with crucial amino acid residues that facilitate both formate and CO_2 binding. Nonetheless, a recent study introduced a new FDH strain, *Thiobacillus sp.* (*Ts*FDH), which exhibited an 84.2-fold increase in CO_2-reducing activity, suggesting promising alternatives in this domain. Furthermore, the study revealed that low pH notably enhanced the CO_2 reduction activity (Choe et al., 2014). In synthetic biology applications, a noteworthy approach involves combining carbonic anhydrase and FDH for carbon reduction through the use of microbial transglutaminase as a cross-linking agent. This hybrid enzyme exhibited improved thermal stability while retaining enzymatic activity. Overall, the catalytic efficiency for formate production increased 5.8 times compared to free FDH (Zhang et al., 2021).

Moreover, the fluctuation of formate levels in bodily fluids under diverse physiological conditions in mammals has paved the way for potential clinical utility of formate dehydrogenase. Comprehensive research is conducted to assess NADH, generated through FDH-mediated reactions, particularly for early detection of vitamin

B12 deficiency and methanol toxicity using spectrophotometric techniques (Martin-Amat et al., 1978, Lamarre et al., 2013, Pietzke et al., 2020)

1.6 Protein Engineering Approaches

In recent times, proteins have gained prominence in driving environmentally friendly processes, reshaping their role in both pharmaceutical and industrial sectors. Industries are seeking enzymes capable of withstanding harsh conditions, including high temperatures and varying pH levels, while prioritizing precision in substrate and cofactor interactions to enhance overall efficiency (Brannigan and Wilkinson, 2002). Simultaneously, protein engineering efforts aim to improve drug-target interactions, minimize side effects, and prolong the duration of effectiveness (Carter, 2011). Protein engineering involves DNA manipulation to modify sequences, resulting in attributes such as increased yield and durability (Brannigan and Wilkinson, 2002). Protein engineering involves three main methods: rational design, directed evolution, and semi-rational design.

1.6.1 Rational Design

Rational design is a protein engineering approach that employs the three-dimensional structure and functional understanding of a protein to manipulate its amino acid sequence. A prominent technique within rational design is site-directed mutagenesis, often performed using commercially available reaction kits optimized for efficiency. This methodology allows targeted modifications in sequence to enhance function or stability based on the protein's structure or homology models when available. Through this technique, amino acid residues can be inserted, deleted, or substituted (Lutz and Iamurri, 2018).

The site-directed mutagenesis approach holds significance in fine-tuning cofactor and substrate affinities, as well as modifying enzyme kinetics (Carter, 1986, Siloto and Weselake, 2012). Similarly, it can investigate the alterations in protein-drug binding and function, offering retrospective insights into the structure-function relationship (Chueh et al., 2002, Yu et al., 2005, Nishi et al., 2009). Although this

method demands individual mutant purification and testing, it is more cost-effective compared to high-throughput alternatives (Reetz et al., 2023).

1.6.2 Directed Evolution

Directed evolution involves modifying a protein's characteristics, including affinity, stability, and specificity, by creating an extensive DNA library designed to facilitate evolutionary changes. This approach requires a pre-existing and validated enzymatic or binding assay to enable efficient monitoring of genotype or phenotypic modifications. Furthermore, these changes must be visibly discernible in terms of phenotype and suitable for screening (Arnold, 1998).

This technique does not require three-dimensional structural information. Diversification is accomplished by creating a DNA library through random mutagenesis. The desired variants are then selected through screening and selection processes. These screening cycles are performed continuously for optimization of the chosen variants (Wang et al., 2021). In directed evolution, gene diversification can be done non-recombinatively with random mutagenesis or recombinatively by modifying gene segments using homologous or non-homologous methods. The screening can be carried out in vitro with automated systems or in a suitable host, such as bacteria or viruses (Zeymer and Hilvert, 2018, Emond and Hollfelder, 2021).

In the non-recombinative approach, random mutations are introduced using techniques like insertion, deletion, and substitution, similar to directed evolution. These mutations can be induced by DNA-damaging agents like mutagens or UV radiation, or by utilizing error-prone PCR. Error-prone PCR employs primers that induce errors, leveraging the inherent probability of errors during DNA replication (Chirumamilla et al., 2001, Arnold, 1998).

In contrast, the recombinative approach mimics the gene alterations observed in sexual reproduction, whether homologous or non-homologous, to create diversity (Stemmer, 1994). In this approach, similar to DNA shuffling, different genes are fragmented and then reassembled through PCR using specially designed primers (Chirumamilla et al., 2001, Arnold, 1998).

1.6.3 Semi-Rational Design

Semi-rational design emerged as a solution that addresses the limitations of both directed evolution's randomness and rational design's cost-inefficiency. This approach combines the advantages of both by utilizing the protein's known structure and in silico predictions. Functionally essential residues are identified, and more targeted libraries are generated through site-saturation mutagenesis (Lutz, 2010, Siloto and Weselake, 2012).

After the screening process, similar to rational design, the most promising variants are selected. These selected variants can be further fine-tuned by site-directed mutagenesis. This technique, performed via PCR with primers that contain codon variations for the identified residues, has been confirmed in various studies (Chica et al., 2005, Carter, 1986).

1.7 Protein Engineering Studies for Formate Dehydrogenase

Initial protein engineering studies concentrated on metal dependent FDHs. However, the attention shifted towards metal independent FDHs due to their higher frequency of study. Metal-dependent FDHs, characterized by complex structures involving heterooligomers and multiple cofactors, present challenges for methods like cryo-EM. Additionally, their lower homology compared to metal independent FDHs adds to these difficulties. Similar to other industrially relevant proteins, protein engineering efforts for FDH have been focused on enhancing catalytic activity, substrate affinity, and thermal stability (Galkin et al., 2002, Calzadiaz-Ramirez and Meyer, 2022).

Efforts aimed at improving CO_2 reduction, similar to other metal-independent FDHs such as *C. thermophilum*, have gained momentum in response to the growing focus in carbon reduction pathways. *Candida boidinii* NAD^+-dependent FDH has gained significant attention for industrial FDH enhancements due to its remarkable thermal stability and catalytic activity, making it a promising candidate (Bulut et al., 2021).

1.7.1 Increasing Enzymatic Activity of Candida boidinii Formate Dehydrogenase

Mutation studies on *Cb*FDH activity have shed light on the significance of residues in substrate and cofactor binding, as well as enzyme activity. For instance, Labrou et al. reported that the Arg258Ala mutation led to a loss of enzyme activity. This outcome underscores the crucial role of Arg258 both in formate binding and hydride transfer. Similarly, the His311Gln mutation, known for its involvement in substrate binding, notably decreased formate binding by a factor of 10, although NAD affinity remained unchanged. The Asn119His and Asn119His/His311Gln double mutants, known for their contribution to NAD^+ binding, significantly reduced the affinity for both NAD^+ and formate by 70-200 times (Labrou and Rigden, 2001).

Mutations Ile175Ala and Phe69Ala, known for their crucial role in shaping the hydrophobic active site, exhibited a similar decrease in formate and NAD^+ affinity. Further investigation unveiled the importance of Pro68 and Phe97, vital for forming the hydrophobic wall, in formate binding (Labrou and Rigden, 2001).

Various *Cb*FDH activity mutation studies have demonstrated distinct outcomes. For instance, Cys23Ser and Phe285Ser mutations increased the activity (Tishkov et al., 2015), while Val120Ser and Asn187Asp mutations decreased it (Jiang et al., 2016). The underlying principle involves converting non-polar residues into polar or charged counterparts, thereby changing electrostatic interactions within the active site due to this polarity shift (Figure 1.5). Notably, the His311Phe mutation hindered both formate binding and activity, perturbing the His311-Gln287 proton-relay mechanism. Moreover, the His311Gln and Gln287Glu mutations lowered the activity (Labrou and Rigden, 2001).

In our previous study, we observed that the His311Gln and Gln287Glu mutants led to improved turnover rates and formate affinity, aligning with Labrou's findings (Bulut et al., 2021). Importantly, our novel *Cb*FDH mutants showed potential for enhancing activity in biotechnological applications. The Val120Thr and Phe285Thr mutants demonstrated substantially higher enzymatic turnover rates and enhanced formate binding affinity, evidenced by lower K_M and higher k_{cat} values(Table 1.1) (Bulut, 2019).

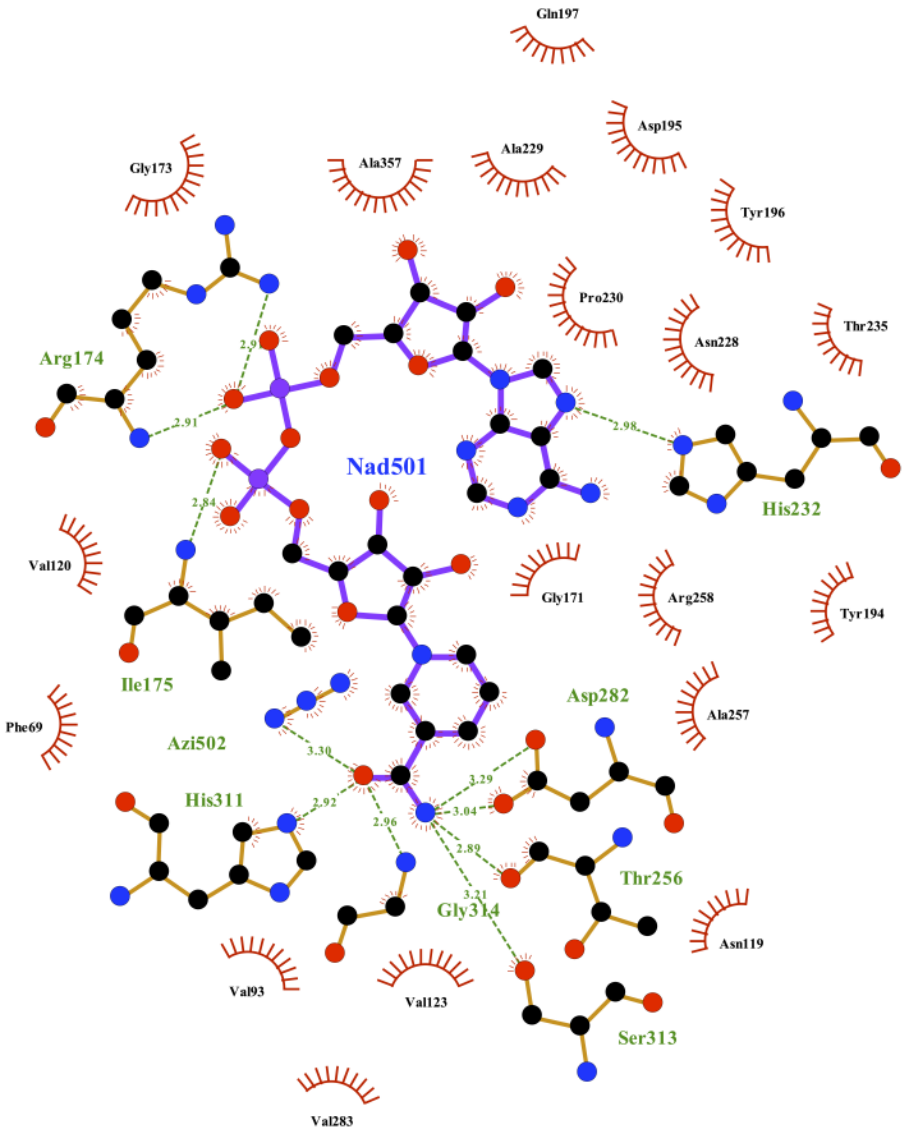

Figure 1.5: A 2D representation of the *Cb*FDH active site. Atoms are shown as colored balls: black for carbon, blue for nitrogen, red for oxygen. The bonds of NAD^+ are colored in purple, while other bonds are in orange. The amino acids that form hydrogen bonds are shown in balls and sticks. The spoked arcs represent the non-bonded interactions.

Table 1.1: Enzyme kinetics of wild-type and mutant *Cb*FDH. (Bulut, 2019)

	Wild-type	**Val120Thr**
$\mathbf{K_M}$ **(mM)**	2.00	1.30
$\mathbf{k_{cat}}$ **(s^{-1})**	9.20 x 10^2	6.23 x 10^3
$\mathbf{k_{cat}/K_M}$	4.74 x 10^2	4.79 x 10^3

1.7.2 Increasing Thermal Stability of Candida boidinii Formate Dehydrogenase

Thermal stability studies on NAD^+-dependent FDH frequently involve manipulation of cysteine residues. For example, mutations such as Cys255Met, Cys255Ser, and Cys255Ala in *Pse*FDH, a homolog of *Cb*FDH, were found to increase the NAD^+ affinity while reducing thermal stability (Tishkov et al., 1993). In the case of *Cb*FDH, Cys23Ser and Cys262Ala mutations similarly resulted in decreased thermal stability, without affecting activity. However, these mutants exhibited enhanced resistance against metal-induced oxidative stress due to their increased stability. This can be attributed to the hydrophilic nature of cysteine making the enzyme more exposed to water and hence more susceptible to the effects of metals (Slusarczyk et al., 2000).

Furthermore, studies have revealed that increasing the hydrophobicity of helical structures through mutations like Ser131Ala, Ser160Ala, Ser184Ala, and Ser228Ala in *Pse*FDH can enhance thermal stability. This approach holds potential to improve the thermal stability of *Cb*FDH as well (Rojkova et al., 1999).

In our previous study, we observed that His311Gln and Gln287Glu mutations in conserved active site residues resulted in a substantial improvement in thermal stability of *Cb*FDH. Circular dichroism analysis revealed a remarkable increase in the enzyme's melting temperature as a result of these mutations. Specifically, the His311Gln mutation raised the melting temperature from 64° (wild-type *Cb*FDH) to 77°, while the Gln287Glu mutation elevated it to 73° (Figure 1.6).

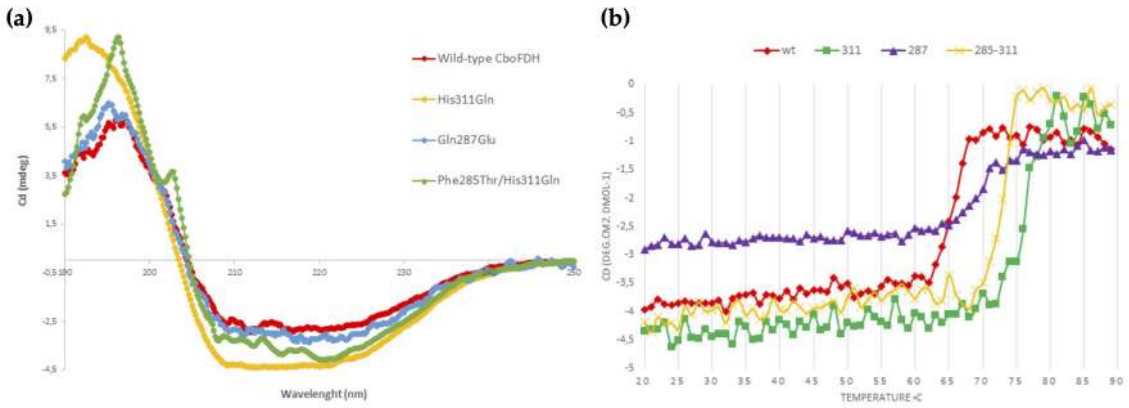

Figure 1.6: (a) Secondary structure analysis of *Cb*FDH variants. (b) Thermal denaturation curves for wild-type and mutant *Cb*FDH between 20-90°C in the spectrum between 190-250 nm. (Bulut et al., 2021)

Moreover, these point mutations also led to a significant increase in the optimal temperature for enzymatic activity by 25-30° (Figure 1.7) (Bulut et al., 2021). This significant increase in temperature tolerance offers valuable prospects for the potential use of *Cb*FDH in biotechnological applications under extreme conditions.

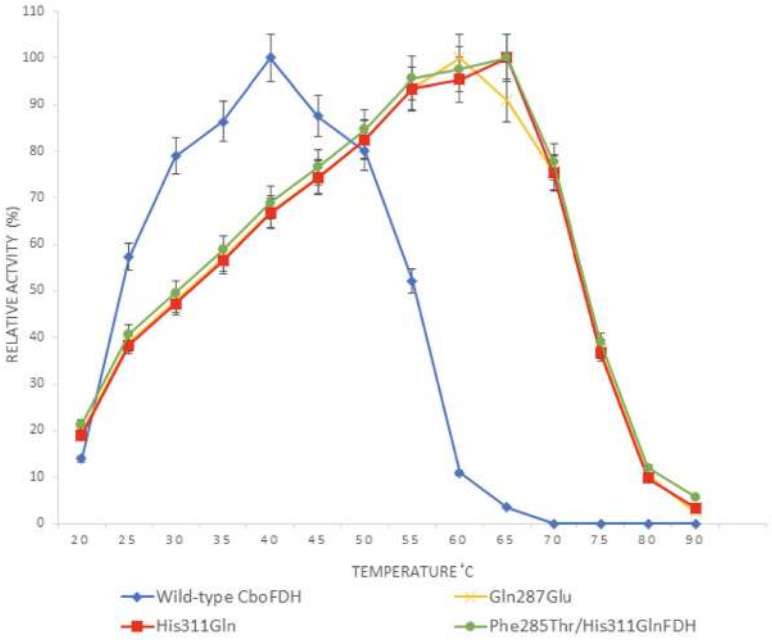

Figure 1.7: Optimum temperature for enzymatic activity of wild-type and mutant *Cb*FDH. (Bulut et al., 2021)

1.8 X-ray Crystallography

X-ray crystallography is the most popular and commonly used technique to determine the structures of biomacromolecules. It allows for obtaining high resolution structures revealing details of molecules at atomic scale.

Structure determination by X-ray crystallography requires the formation of protein crystals. The crystal quality of a protein depends on various factors (Chayen and Saridakis, 2008). In order to obtain high-quality crystals, the protein should be obtained with the highest purity possible. Therefore, proteins are usually purified several times using different techniques such as affinity, ion exchange and size-exclusion chromatography. Another factor is the stability of the protein. A protein that is stable in a solution will easily stabilize in its low energy state and form crystals. An unstable protein, on the other hand, will likely aggregate and precipitate. The concentration of the protein is also a very important factor affecting the crystal formation and quality. At low concentration, the protein cannot reach the supersaturated state to form crystals while concentrations that are too high leads to precipitation (Weber, 1991).

In order to drive the proteins to their supersaturated state (Figure 1.8) for crystallization, different crystallization screen solutions and techniques are used. The crystallization screens offer varying environmental conditions such as pH, precipitant, and salts in order to increase the chance of crystal formation (Weber, 1991). To find the best condition for a protein to crystallize, the protein is usually screened against numerous solutions, called sparse matrix screens that are commercially available.

There are various methods used for protein crystallization. The most common method is vapor diffusion in which crystals are grown due to a concentration gradient between protein-solvent mixture and a reservoir of solvent (McPherson, 2017). The solvent evaporates from the mixture and diffuses into the reservoir. As a result, the protein concentration in the mixture increases and eventually reaches supersaturation. Vapor diffusion has two main types of setups: sitting drop and hanging drop. In sitting drop, the drop of protein solution sits on a pedestal above the

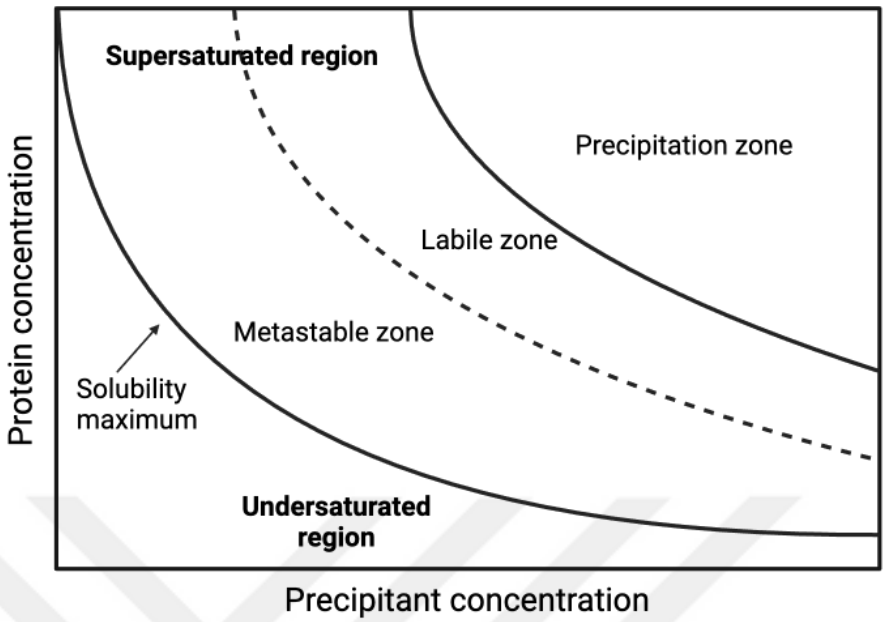

Figure 1.8: Phase diagram for crystallization. The black arrow indicates the maximum solubility. The solid lines divide the phases, while the dashed line separates the supersaturated region into two regions. Crystals nucleate and grow in the labile region, whereas they cannot nucleate but grow in the metastable region.

reservoir. In hanging drop, the drop is hanging on a cover slip that is placed above the reservoir. Both setups must be closed in order to prevent evaporation from the reservoir (McPherson, 2017).

In this study, the sitting drop vapor diffusion microbatch under oil method is used (Figure 1.9) (Ertem et al., 2022). In this method, a small drop of the protein solution is mixed with equal volume of crystallization screen in a well of a Terasaki plate. The mixture is then covered with a drop of paraffin oil to slow down evaporation. This process is repeated for all available screens.

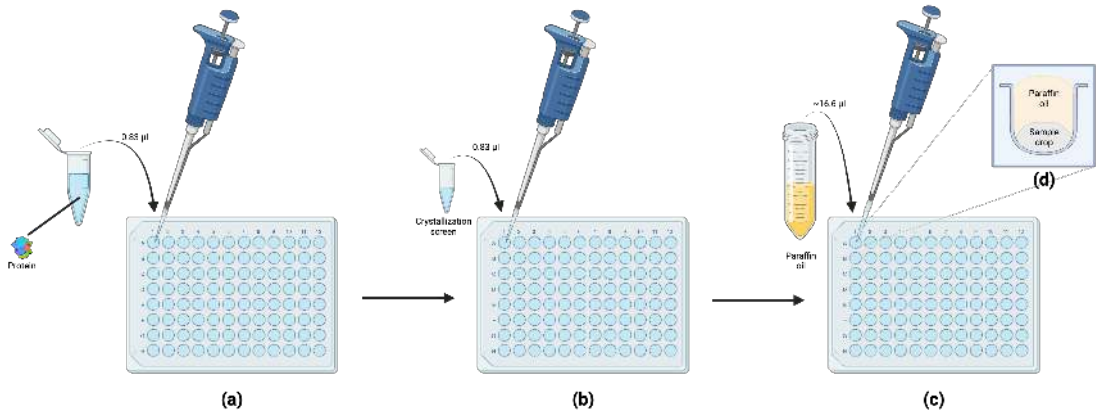

Figure 1.9: Sitting drop vapor diffusion microbatch under oil method. (a) Protein solution is added to the well. (b) Crystallization screen is mixed with the protein solution in the well. (c) Sample drop is covered with oil. (d) Side view of a well containing the sample drop covered with paraffin oil.

Chapter 2

MATERIALS AND METHODS

2.1 Materials and Equipment

2.1.1 LB Medium, Stock Antibiotics and IPTG

LB medium (Table 2.1) and stock solutions of antibiotics and 0.4 M IPTG (Table 2.2) were prepared to be used in transformation and protein expression experiments.

Table 2.1: LB Medium

Reagent	**Amount (g/L)**
Tryptone	10
NaCl	10
Yeast extract	5
Total	25

Table 2.2: Antibiotic and 0.4 M IPTG Stock Solutions

Reagent	**Amount (mg/ml)**
Ampicillin	100
Chloramphenicol	35
IPTG	95.324

2.1.2 Buffers

For small-scale expression check and protein purification, lysis buffer (Table 2.3), HisA buffer (Table 2.4), and HisB buffer (Table 2.5) were prepared.

Table 2.3: Lysis Buffer

Reagent	**Final concentration**	**Amount**
NaCl	500 mM	29.22 g
Tris	50 mM	6.06 g
Glycerol	5% (v/v)	50 ml
Triton X-100	0.5% (v/v)	5 ml
Imidazole	20 mM	1.362 g
ddH_2O		up to 1 L
Total		1 L

Table 2.4: HisA Buffer

Reagent	**Final concentration**	**Amount**
NaCl	200 mM	11.688 g
Tris	20 mM	6.06 g
Imidazole	20 mM	1.362 g
ddH_2O		up to 1 L
Total		1 L

Table 2.5: HisB Buffer

Reagent	**Final concentration**	**Amount**
NaCl	200 mM	11.688 g
Tris	20 mM	6.06 g
Imidazole	250 mM	17.019 g
ddH_2O		up to 1 L
Total		1 L

2.2 Bacterial Transformation

Full-length wild-type and Val120Thr mutant *C. boidinii* formate dehydrogenase genes were previously cloned into an empty pET-23a (+) bacterial expression vector by Bulut et al (2021). The constructs include a non-cleavable C-terminal hexahistidine tag for affinity chromatography (Figure 2.1). The amino acid sequences of the *Cb*FDH constructs are given below. The hexahistidine tag is indicated with bold text, while the mutation site is indicated between asterisks.

Wild-type *Cb*FDH:

MKIVLVLYDAGKHAADEEKLYGCTENKLGIANWLKDQGHELITTSDKE
GGNSVLDQHIPDADIIITTPFHPAYITKERIDKAKKLKLVVVAGVGSDHID
LDYINQTGKKISVLEVTGSNVVSVAEHVLMTMLVLVRNFVPAHEQIINH
DWEVAAIAKDAYDIEGKTIATIGAGRIGYRVLERLVPFNPKELLYYDYQ
ALPKDAEEKVGARRVENIEELVAQADIVTINAPLHAGTKGLINKELLSK
FKKGAWLVNTARGAICVAEDVAAALESGQLRGYGGDVWFPQPAPKDH
PWRDMRNKYGAGNAMTPHYSGTTLDAQTRYAEGTKNILESFFTGKFD
YRPQDIILLNGEYITKAYGKHDKK**HHHHHH**

***Cb*FDH-Val120Thr:**

MKIVLVLYDAGKHAADEEKLYGCTENKLGIANWLKDQGHELITTSDKE
GGNSVLDQHIPDADIIITTPFHPAYITKERIDKAKKLKLVVVAGVGSDHID
LDYINQTGKKISVLEVTGSN*T*VSVAEHVLMTMLVLVRNFVPAHEQIIN
HDWEVAAIAKDAYDIEGKTIATIGAGRIGYRVLERLVPFNPKELLYYDYQ
ALPKDAEEKVGARRVENIEELVAQADIVTINAPLHAGTKGLINKELLSK
FKKGAWLVNTARGAICVAEDVAAALESGQLRGYGGDVWFPQPAPKDH
PWRDMRNKYGAGNAMTPHYSGTTLDAQTRYAEGTKNILESFFTGKFD
YRPQDIILLNGEYITKAYGKHDKK**HHHHHH**

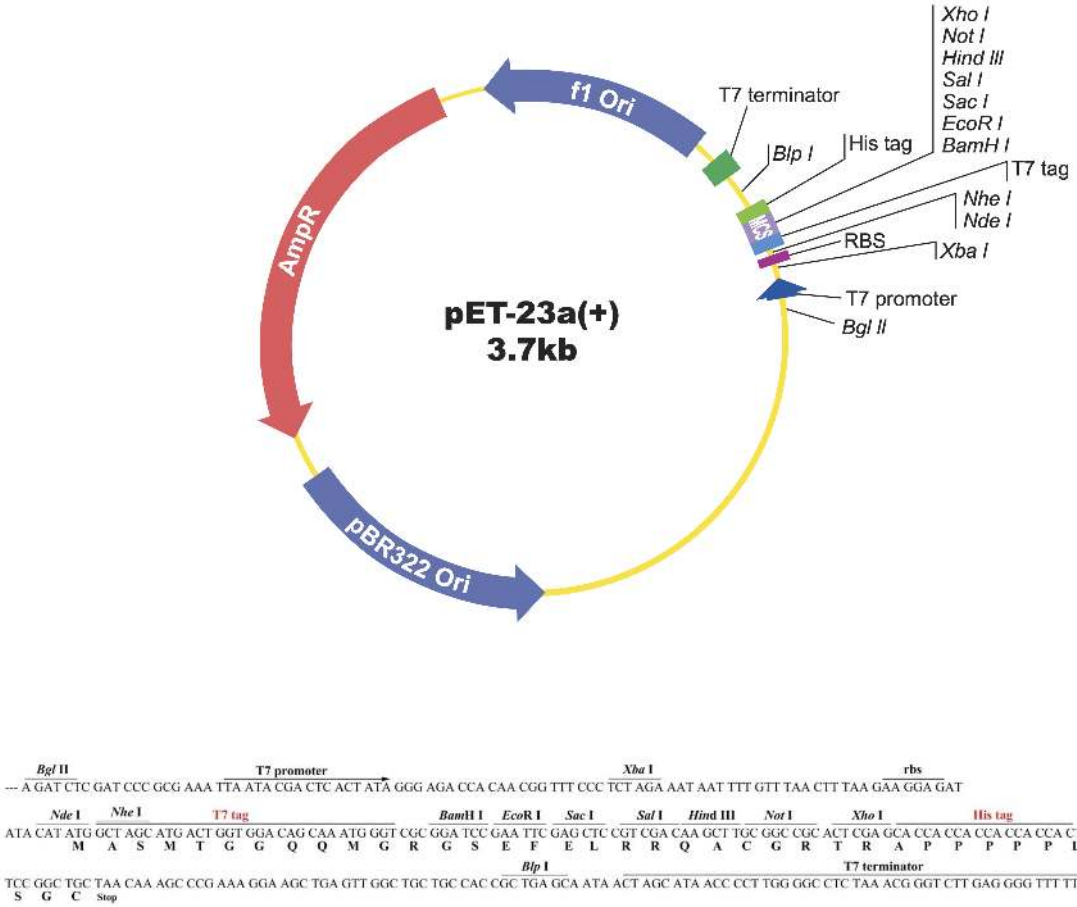

Figure 2.1: The plasmid map of the bacterial expression vector pET-23a(+). AmpR indicates the ampicillin resistance gene. MCS stands for multiple cloning site. (GenScript, USA)

The cloned vector was transformed into competent *Escherichia coli* BL21 Rosetta-2 cells. Both the competent cells and plasmid vector were thawed on ice for 20 minutes. 50 µl of the competent cells were mixed with 2 µl of plasmid in a sterile Eppendorf tube by gently pipetting up and down. The mixture was incubated on ice for another 20 minutes. The bacterial cells were then exposed to heat shock on a heat block at 42°C for 45 seconds. After heat shock, the tube was placed on ice for 2 minutes. Then, 500 µl of room-temperature LB medium was added to the mixture. The cells were incubated at 37°C for 90 minutes, the tube was inverted several times in 15–20-minute intervals.

After incubation at 37°C, the tube was centrifuged at 1500 rpm (238g) for 2 minutes. The supernatant was discarded by inverting the tube once. The pellet

was resuspended in the remaining supernatant by pipetting. 50 µl of the cells were pipetted onto an agar plate in a fume hood sterilized beforehand. The cells were spread on the plate by adding a few spreader beads and rocking the plate back and forth. After removing the beads, the plate was covered with the lid, placed upside down in a 37°C incubator and incubated overnight.

7 ml LB medium was added to a sterile flask. 7 µl ampicillin and 7 µl chloramphenicol were added to the LB medium for double antibiotic selection. As pET-23a (+) vector has resistance to ampicillin and Rosetta-2 cells to chloramphenicol, we expect the transformed cells to grow in a medium containing these antibiotics. The colonies grown on the agar plate overnight was taken with a micropipette and inoculated into the LB medium. The cell culture was incubated at 37°C at 110 rpm for 5-6 hours.

After incubation, 750 µl sterilized 80% glycerol and 750 µl cell culture were added into a cryotube and mixed by vortexing. The glycerol stocks were stored at -80°C.

2.3 Small-scale Expression Check

10 ml of LB (30 g/L) medium was prepared for each *Cb*FDH variant and autoclaved at 121°C for 20 minutes. 5 ml ampicillin (100 mg/ml stock) and 5 ml chloramphenicol (35 mg/ml stock) antibiotics were added into LB medium. The final antibiotic concentration is 100 µg/ml and 35 µg/ml, respectively.

Glycerol stocks containing the *Cb*FDH constructs were inoculated into the prepared LB media. The cell cultures were incubated at 37°C with continuous shaking at 110 rpm overnight (18-24 hours). After overnight incubation, 3 ml "before induction" sample from each cell culture was taken and centrifuged. The supernatant was discarded, and the cells were stored at -45°C until the pulldown experiment.

To induce protein expression, 7 µl 0.4 M IPTG (isopropyl β-D-1-thiogalactopyranoside) was added to each of the remaining cultures. The final IPTG concentration is 0.4 mM. The cultures were further incubated at 37°C and 110 rpm for 4 hours. Following IPTG induction, the cells were harvested by centrifugation at 3500 rpm for 30 minutes.

The cell pellets were resuspended in 1 ml lysis buffer (see Table 2.3) and sonicated until completely dissolved. The cell lysates were then centrifuged at 10000 rpm for 15 minutes. The supernatants were transferred into clean tubes. 40 µl Ni-NTA beads were added into each tube. After incubation with the beads at 4°C for 4-5 hours, the samples were centrifuged at 2400 rpm for 2.5 minutes. The supernatants were carefully discarded.

1 ml HisA buffer (see Table 2.4) was added into each tube and incubated for 30 minutes. The samples were centrifuged at 2400 rpm for 2.5 minutes, and the supernatants were discarded. 200 µl HisB buffer (see Table 2.5) was added into each tube and incubated for 2-3 minutes for eluting the protein from the beads.

2.4 Large-scale Protein Production and Purification

150 ml and 6 x 750 ml LB media were prepared and autoclaved for sterilization. 150 µl ampicillin stock solution and 150 µl chloramphenicol stock solution were added into the sterilized 150 ml LB medium. A piece of the frozen glycerol stock from -80°C was taken with a pipette tip and inoculated into the LB medium. The inoculated cells were incubated at 37°C at 110 rpm overnight (18-24 hours).

Next day, 750 µl ampicillin and 750 µl chloramphenicol were added into each flask containing 750 ml LB medium. The overnight grown culture was split into these 6 flasks which were again incubated at 37°C at 110 rpm. Every hour the OD600 of the cultures were measured using a NanoDrop device. When the OD600 reached around 0.7-0.8, 750 µl 0.4 M IPTG was added into each flask for induction. The cultures were induced for 4 hours at 37°C at 110 rpm.

After incubation, the cultures were centrifuged at 3500 rpm for 45 minutes and the supernatants were discarded. Most of the cells were harvested from the centrifuge bottles using a spoon and collected into falcon tubes. The rest of the cells were collected by dissolving in a few milliliters of LB. Then, the falcon tubes were centrifuged at 3500 rpm for 30 minutes and the supernatants were discarded. The harvested cell pellets were stored at -45°C until purification.

A big ice box was filled with crushed ice. The cell pellets were taken from

the -45°C freezer and put on ice. Lysis buffer (see Table 2.3) was added on top of the cell pellets up to 45 ml level on the falcon tube. The cells were sonicated according to the protocol in Table 2.6. The protocol was repeated until the pellets completely dissolved. To avoid overheating, the samples were incubated on ice between sonication rounds.

Table 2.6: Sonication protocol for each round.

Total time	30 s
"On" time	1 s
"Off" time	1 s
Amplitude	60%

After sonication, the cell lysates were transferred into ultracentrifuge tubes, which were then balanced on a weighing device. The cell lysates were centrifuged using a Ti45 rotor in a Beckman Optima™ L-80XP Ultracentrifuge (Beckman, USA) at 35000 rpm at 4°C for 1 hour. After centrifugation, the supernatants were filtered through a filter paper and transferred into a sterilized glass bottle.

The supernatant was applied to a Ni-NTA affinity column mounted to an AKTA go (Cytiva, USA) FPLC device. The column was first equilibrated with HisA buffer (see Table 2.4) until the UV absorbance on the chromatogram became stable. Then, the supernatant was loaded to the column while the flowthrough containing unbound proteins was collected from the outlet valve. The column was again washed with HisA buffer to remove the unbound and nonspecifically bound proteins until the UV absorbance stabilized. Once the UV absorbance was stable, HisB buffer (see Table 2.5) was applied to the column to elute *Cb*FDH. The eluted protein was flash-frozen in liquid nitrogen and stored at -80°C until used.

2.5 Protein Crystallization and Crystal Harvesting

Sitting drop microbatch under oil crystallization screening was performed for the wild-type and mutant *Cb*FDH proteins using commercially available sparse matrix

crystallization screening sets. Equal volumes (0.83 µl) of the protein solution and crystallization screen were mixed in the wells of 72-well Terasaki plates. Each drop was covered with a drop (approximately 16.6 µl) of paraffin oil. Approximately 3500 crystallization conditions were screened for each protein construct. Two crystallization sets were prepared for both proteins to increase the chance of crystal growth. One set was stored at +4°C while the other was at room temperature. The best crystals were grown in Wizard III (Hampton Research, USA) condition number #47 for both the wild-type and mutant *Cb*FDH at +4°C. In order to obtain more crystals, the crystallization experiments were replicated using the same condition in all wells of a Terasaki plate.

For cryogenic data collection, the *Cb*FDH crystals were picked using MiTeGen MicroLoops attached to a magnetic wand (Garman and Owen, 2006) under a light microscope (Atalay et al., 2023). The picked crystals were rapidly frozen by submerging in liquid nitrogen and placed in a robotic sample puck (Cat#M-CP-111-021, MiTeGen, USA) that was priorly cryo-cooled in liquid nitrogen. The data collection at ambient temperature was performed directly from the Terasaki plate in which the crystals were grown.

2.6 X-ray Data Collection and Processing

For cryogenic data collection, the robotic sample puck containing the harvested *Cb*FDH crystals was attached to a puck transfer and mounting tool. Then, it was transferred from the storage dewar into the sample dewar filled with liquid nitrogen at 100 K, of the Turkish Light Source X-ray Diffractometer, *"Turkish DeLight"*.

Diffraction data from the frozen *Cb*FDH crystals using Rigaku XtaLAB Synergy Flow X-ray Diffractometer "Turkish Light Source" (University of Health Sciences, Istanbul, Türkiye). CrysAlis Pro software suite (version 1.171.42.35a) was utilized to control and perform the data collection (Rigaku, Japan). Oxford Cryosystems Cryostream 800 Plus was set to 100 K for constant cooling of the crystals. The X-ray generator (PhotonJet-R) was operated at 40 kV, 30 mA, 1200 W. The data collection wavelength was 1.54 Å. The beam intensity was set to 10%. The data

collection was performed using the same protocol for both wild-type and mutant protein crystals. The detector distance was adjusted to 47.00 mm. The crystals were exposed to X-rays for 10 minutes each time while changing the scan width by 0.25 degrees.

For ambient temperature data collection, the Oxford Cryosystems Cryostream 800 Plus was set to 300 K. The Terasaki plate containing the crystals was mounted to the *XtalCheck-S* plate reader (Gul et al., 2023) module attached to the goniometer omega stage. The detector distance was set to 100.00 mm. Diffraction data was collected from a single crystal with 5 sec exposure time and 1.00 degree oscillation. The plate was oscillated 22.5 degrees in total.

The cryogenic temperature data was processed using the automatic data reduction tool in the CrysAlis Pro software, which generated an mtz file. Each step of the ambient temperature data was checked by peak finding and masking, and the ones with unsuitable unit cells were manually removed. The **xx proffitbatch** command was entered in the command shell to create a batch script for cumulative data reduction. The batch script was run by typing **script** in the command shell. Each data reduction generated an rrprof file containing all unmerged and unscaled data. The **proffit merge** tool embedded in CrysAlis Pro was used to merge all the reduced data and exported an mtz file.

2.7 Structure Determination and Refinement

Molecular replacement for all *Cb*FDH structures was performed using the automated molecular replacement tool PHASER (McCoy et al., 2007) found in the PHENIX software package (Adams et al., 2010). For the wild-type *Cb*FDH structures, a previously determined crystal structure (PDB ID: 5DNA) was used as initial search model. For the Val120Thr mutant, the wild-type structure was first mutated in PyMoL version 2.3 software (Schrödinger, LLC, 2015) and used as search model.

Using PHENIX, the initial rigid-body and simulated annealing refinements were performed based on the model coordinates. Afterward, individual coordinates and translation/libration/screw (TLS) parameters were refined with PHENIX. The re-

fined model was checked on COOT (Emsley and Cowtan, 2004) after every refinement run. The altered side chains and water molecules that were out of the electron density were fixed manually. Water molecules with no or negative density were removed.

The structural alignments were done in PyMoL. The root-mean-square deviation (RMSD) scores were determined based on the fitting of Ca atoms. The figures were generated in PyMoL, COOT, LigPlot^{+} (Laskowski and Swindells, 2011), and BioRender.

Chapter 3

RESULTS

3.1 Expression of Wild-type and Mutant CbFDH

The transformed *E. coli* BL21-Rosetta 2 cells were grown in multiple colonies on agar plates containing ampicillin and chloramphenicol antibiotics, showing the success of transformation. In order to see whether the *Cb*FDH constructs were expressed in the transformed bacteria, small-scale protein expression and pulldown assay were performed before large-scale protein production.

The small-scale protein expression check results demonstrate that all *Cb*FDH constructs were successfully overexpressed in *E. coli* Rosetta-2 cells with IPTG induction at 37°C for 4 hours (Figure 3.1). The "after-induction" samples exhibited a thick protein band around 41 kDa, whereas the "before-induction" samples did not.

Following the positive results of the initial small-scale expression check, each *Cb*FDH construct was expressed in 6 L of LB medium at the same conditions for large-scale production. We were able to obtain wild-type and Val120Thr mutant *Cb*FDH with high purity (Figure 3.1). The monomeric form of the protein is observed as a tick band at 41 kDa while the dimer is also visible around 82 kDa.

In the purification process, a portion of the protein remained in the pellet and flowthrough. Nonetheless, the high protein concentration in the elution samples indicates that some protein might have remained within the cells due to incomplete cell lysis. Moreover, during purification, a fraction of the protein molecules might not have bound to the column due to column saturation. It is also plausible that some of the protein may have aggregated due to high concentration.

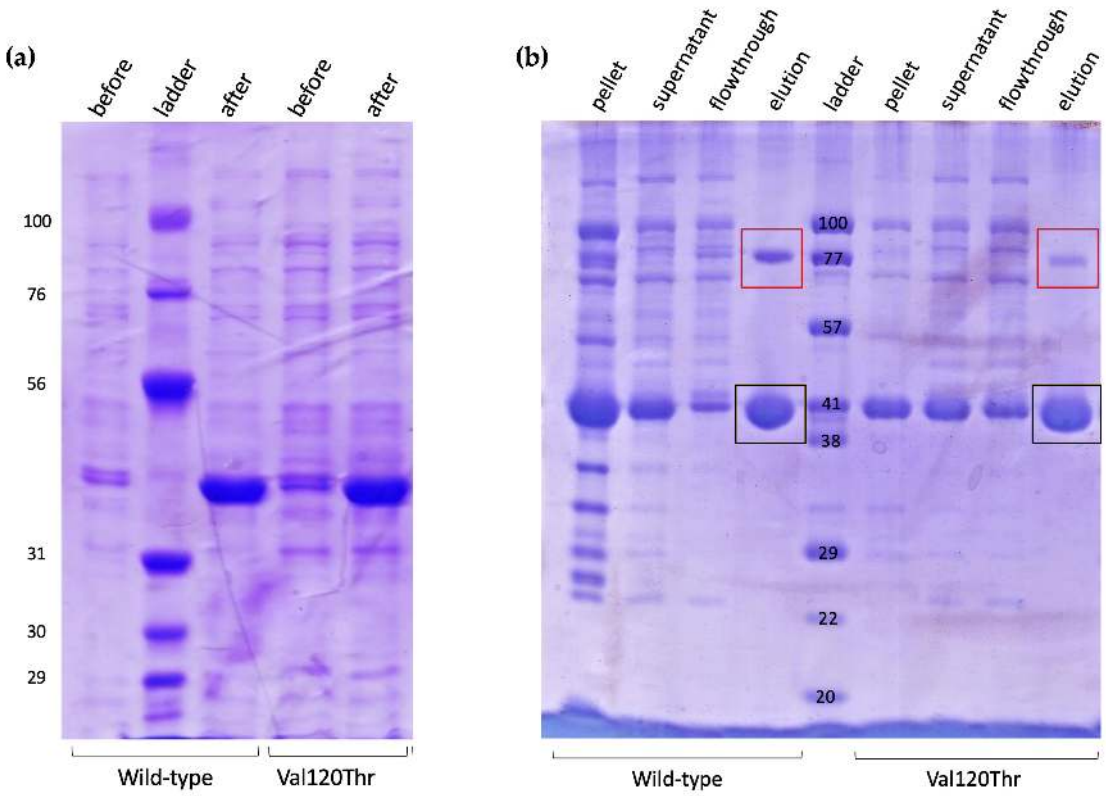

Figure 3.1: Small-scale expression check results for *Cb*FDH constructs. On top, "before" and "after" labels indicate before and after IPTG induction. The construct names are indicated at the bottom. Ladder indicates the protein ladder for size comparison.

3.2 Crystallization of Wild-type and Mutant CbFDH

The wild-type and Val120Thr mutant *Cb*FDH proteins were crystallized using the sitting-drop vapor diffusion microbatch under oil technique. Both protein constructs were screened against approximately 3500 sparse matrix crystallization conditions. The screening was performed both at +4°C and room temperature. The crystals were obtained at +4°C for all of them, while they precipitated within a few days at room temperature. Both wild-type and mutant forms of *Cb*FDH crystallized in the same crystallization condition. The crystals were grown in Wizard III condition #47 (Hampton Research, USA), which comprises 30% (w/v) PEG 5000 MME, 100 mM MES/Sodium hydroxide pH 6.5, and 200 mM Ammonium sulfate.

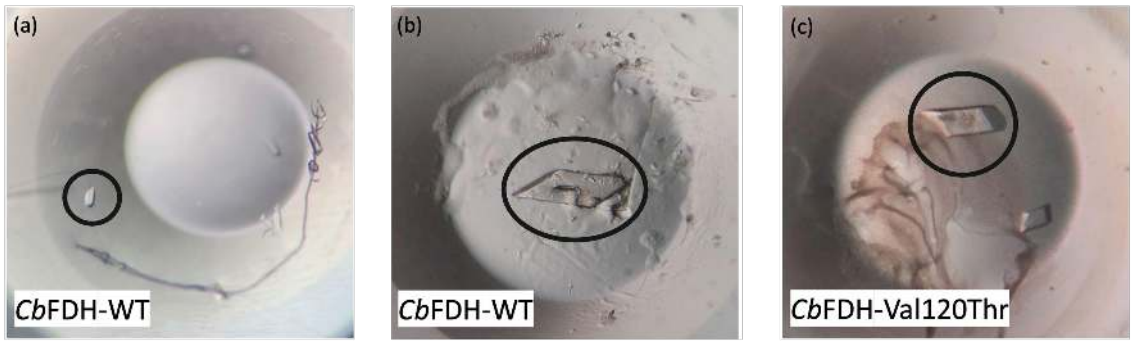

Figure 3.2: *Cb*FDH crystals under microscope. The crystals used for data collections are indicated in black circles. (a) Wild-type *Cb*FDH crystal used in cryogenic temperature data collection, (b) Wild-type *Cb*FDH crystal used in ambient temperature data collection, (c) *Cb*FDH-Val120Thr crystal.

The best-diffracting crystals (Figure 3.2) were then used for X-ray diffraction data collection to determine the protein structure (Figure 3.3).

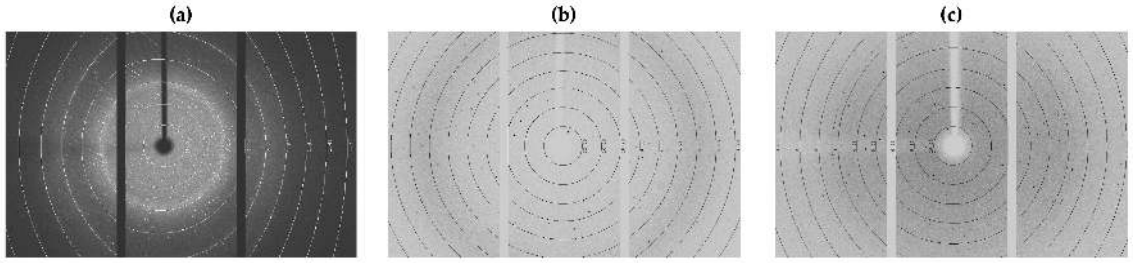

Figure 3.3: A frame from diffraction pattern of (a) wild-type *Cb*FDH at cryogenic temperature, (b) wild-type at ambient temperature, and (c) Val120Thr mutant at cryogenic temperature.

3.3 Structural Analysis of Wild-type and Val120Thr Mutant CbFDH

3.3.1 Cryogenic Temperature Structure of Wild-type Apo CbFDH Structure at 1.4 Å Resolution

The crystal structure of the wild type apo *Cb*FDH was determined at 1.4 Å resolution (PDB ID: 8HTY) at cryogenic temperature (Figure 3.4). The structure, composed of two homodimers, has an overall completeness of 98.82%. According to the Ramachandran statistics, the favored regions consist of the 98.01% of the

residues while 1.99% of those are in the allowed regions. There were no Ramachandran outliers among the residues. Table 3.1 demonstrates the data collection and refinement statistics.

Table 3.1: Data collection and refinement statistics. The highest resolution shell is shown in parentheses. Wt-*Cb*FDH-CT: cryogenic temperature structure; Wt-*Cb*FDH-AT: ambient temperature structure.

Dataset	**Wt-*Cb*FDH-CT**	**Wt-*Cb*FDH-AT**	**Val120Thr-*Cb*FDH**
PDB ID	8HTY	8IQ7	8IVJ
Data collection			
X-ray source	*Turkish DeLight*	*Turkish DeLight*	*Turkish DeLight*
Temperature (K)	100	298	298
Space group	P 1	P 1	P 1
Cell dimensions			
a, b, c (Å)	54.13, 68.95, 109.79	54.66, 69.50, 110.80	53.66, 68.61, 109.43
α, β, γ (°)	78.13, 89.48, 81.11	77.86, 89.05, 81.20	77.96, 89.62, 81.40
Resolution	24.75-1.39 (1.51-1.39)	30.73-2.10 (2.15-2.10)	25.42-1.90 (1.94-1.90)
CC1/2	0.999 (0.340)	0.916 (0.074)	0.622 (0.535)
*CC**	1.000 (0.708)	0.978 (0.372)	0.876 (0.835)
$I/\sigma I$	11.74 (0.73)	7.90 (0.60)	3.00 (0.43)
Completeness (%)	98.82 (86.0)	85.90 (77.30)	99.7 (99.5)
Redundancy	151.46 (148.36)	7.50 (3.30)	7.30 (4.60)
Refinement			
Resolution	21.83-1.40 (1.43-1.40)	30.70-2.10 (2.15-2.10)	24.30-1.90 (1.95-1.90)

No. reflections	301717 (29123)	67181 (4741)	96104 (7897)
R_{work} / R_{free}	0.167/0.190 (0.380/0.372)	0.2433/0.2716 (0.4364/0.4810)	0.2469/0.2712 (0.4052/ 0.4226)
No. atoms			
Protein	22225	22154	22275
Ligand / Ion / Water	2249	393	1459
B-factors			
Protein	22.94	18.89	22.47
Ligand / Ion / Water	35.07	17.02	26.27
Coordinate errors	0.18	0.38	0.30
R.m.s deviations			
Bond lengths (Å)	0.015	0.002	0.002
Bond angles (°)	1.422	0.545	0.568
Ramachandran plot			
Favored (%)	97.4	97.66	98.02
Allowed (%)	2.6	2.34	1.98
Disallowed(%)	-	-	-

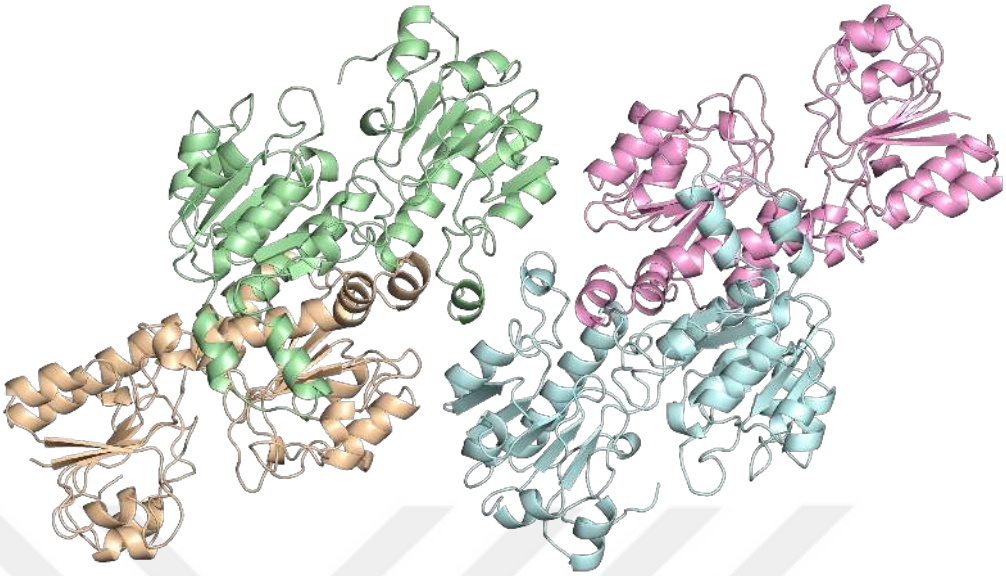

Figure 3.4: 1.4 Å apo wild-type *Cb*FDH structure as two homodimers. Four monomer molecules are shown in different colors.

The atomic 1.4 Å resolution provides a high-quality electron density map that reveals structural details including amino acid side chains, water molecules, and buffer components, such as sulfate ions and MES. It remains visible and intact without any breaks at higher sigma levels (Figure 3.5).

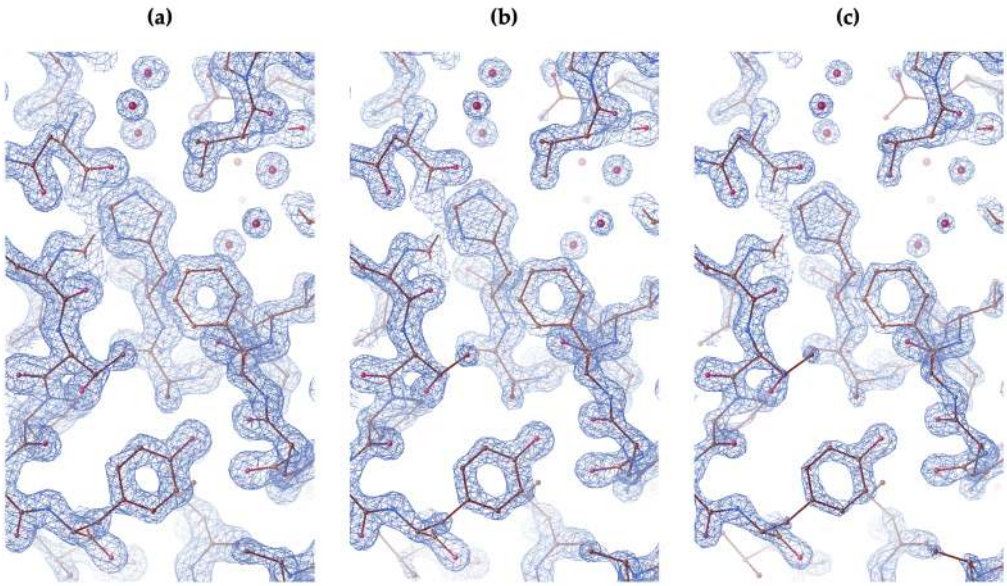

Figure 3.5: 2Fo-Fc map is contoured at **(a)** 2.0 σ, **(b)** 2.5 σ, and **(c)** 3.0 σ level. *Cb*FDH is demonstrated in stick representation.

The two homodimers that make up the crystal structure were superposed for comparison (Figure 3.6). The resulting RMSD value was 0.35, showing that the homodimers align well with minor differences. A closer look at the dimerization regions with the homodimers reveal that these regions fit perfectly on each other. Slight differences are observed in the more flexible regions that do not contribute to dimerization, resulting in a small RMSD score.

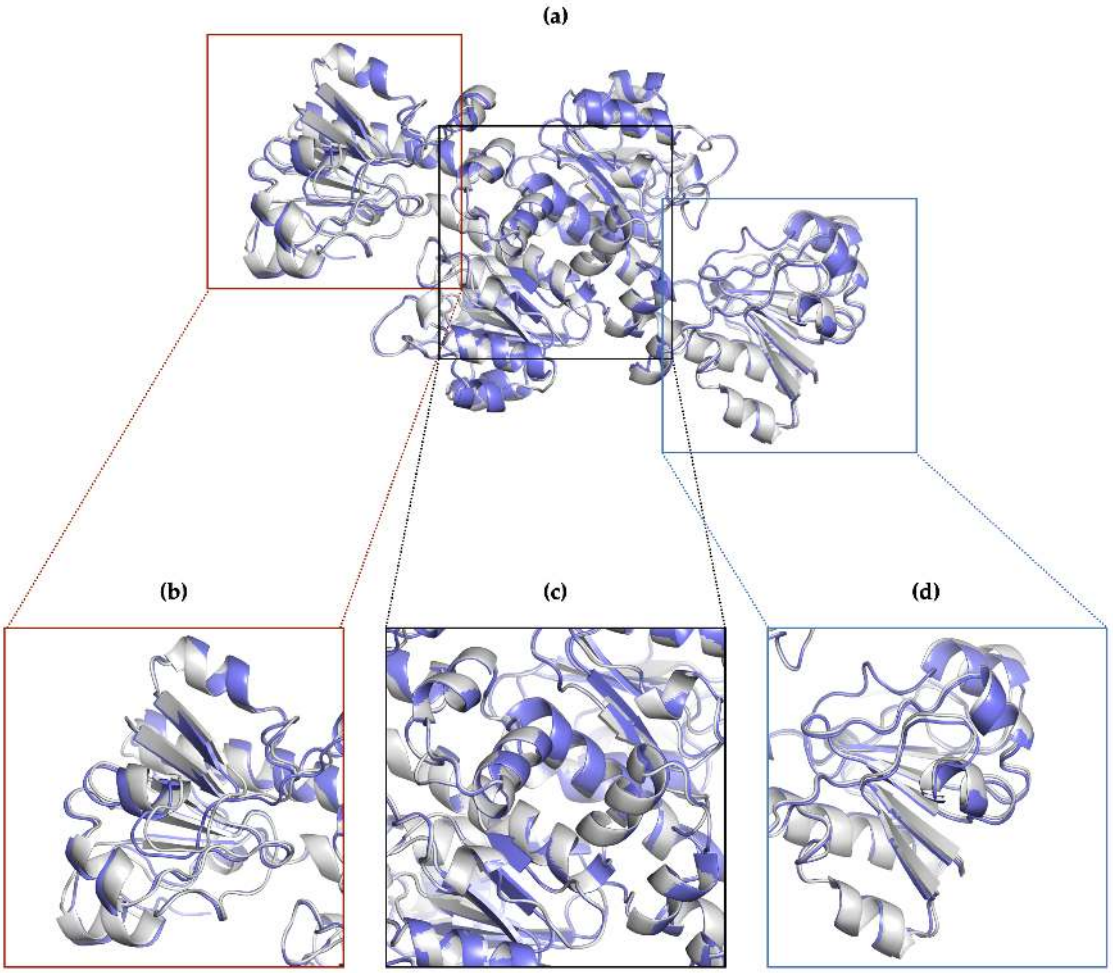

Figure 3.6: Alignment of two *Cb*FDH homodimers. **(a)** Superposition of homodimers. One homodimer is shown in slate, and the other in gray. **(b)**,**(d)** Regions that are farther from the dimerization site. **(c)** Dimerization region.

In order to see whether there is any structural differences in our cryogenic apo wild type *Cb*FDH structure, we superposed our structure with a previously determined apo wild type *Cb*FDH at cryogenic temperature with a 1.75 Å resolution

(PDB ID: 5DNA) (Guo et al., 2016). The superposition resulted in an RMSD score of 0.26 Å, indicating that there is no significant difference between the two structures (Figure 3.7).

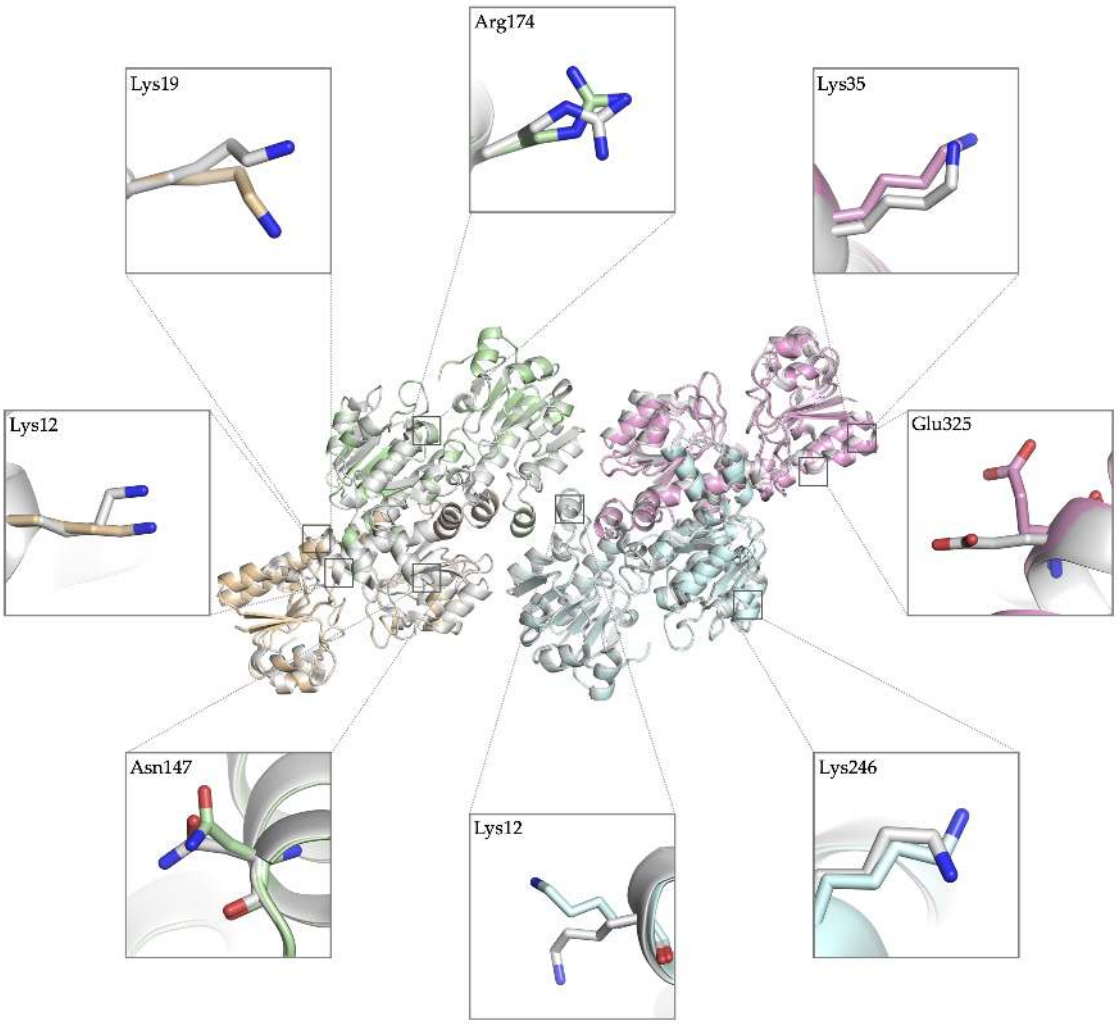

Figure 3.7: Two apo wild type *Cb*FDH structures are superposed. Our structure (8HTY) is in four colors indicating each monomer; A: pale green, B: wheat, C: pink, D: pale cyan. 5DNA is shown in gray. Side chain differences are shown in black squares.

Most of the differences are observed in the residues that are directly exposed to the solvent (Figure 3.7). Additionally, all residues in our *Cb*FDH structure have well-defined electron density while the previous apo *Cb*FDH structure has missing residues in its chain C (Figure 3.8).

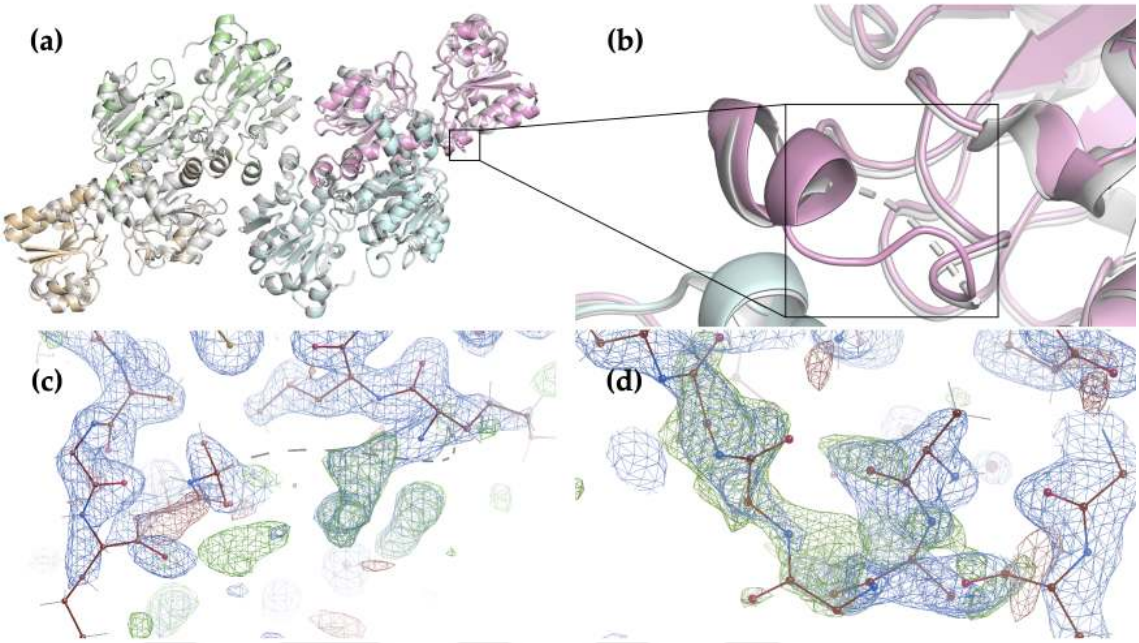

Figure 3.8: Comparison of the residues 15-18 in chain C of 8HTY and 5DNA. **(a)** Superposition of 8HTY and 5DNA. The residues 15-18 are indicated in a black square. 8HTY is shown in four colors: pale green, wheat, pink, pale cyan. 5DNA is shown in gray. **(b)** Residues 15-18. The missing residues of 5DNA are indicated with dashed line. **(c)** 2Fo-Fc (in slate) and Fo-Fc (in green) maps of chain C of 5DNA residues 14 and 19. Dashed lines represent the missing residues. **(d)** 2Fo-Fc and Fo-Fc maps of the chain C residues 14-19 of 8HTY.

3.3.2 Comparison of Apo and Holo Wild-type CbFDH Structures

The cryogenic temperature structure of the wild-type *Cb*FDH (PDB ID: 8HTY) was aligned with a previously determined holo *Cb*FDH structure (PDB ID: 5DN9) (Guo et al., 2016) in order to see the conformational differences in the absence and presence of the coenzyme and substrate/inhibitor molecules. This holo structure includes the coenzyme NAD^+, the inhibitor azide mimicking the substrate, and a chloride ion. The calculated RMSD score of this superposition is 1.80 Å, revealing significant conformational variations between the two structures (Figure 3.9).

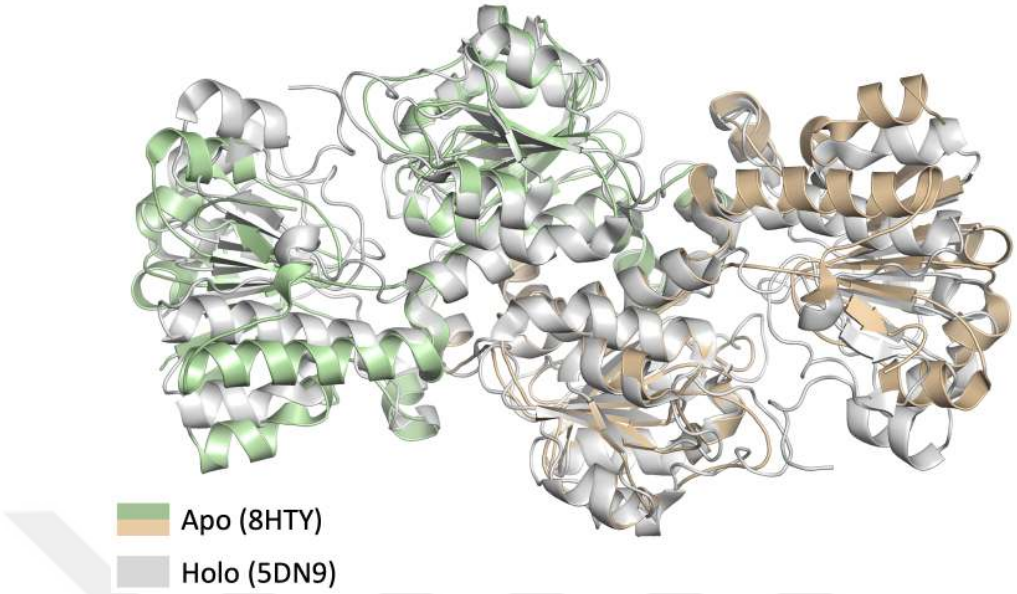

Figure 3.9: Superposition of apo (PDB ID: 8HTY) and holo (PDB ID: 5DN9) wild-type *Cb*FDH structures. Monomers of the apo structure are colored in pale green and wheat. The holo structure is colored in gray.

Conformational variations were observed not only in the flexible loop regions, but also in domains encompassing multiple α-helices and β-sheets. Morph analysis was conducted to elucidate how conformation of the *Cb*FDH is altered upon binding of the coenzyme NAD^+ and inhibitor azide (Ohyama and Yamazaki, 1975). The apo *Cb*FDH structure was utilized as the starting point, while the holo structure represented the final conformation. The morph analysis unveiled that the binding of NAD^+ and azide induces major conformational shifts. The binding event brings the two domains of each monomer come closer, resulting in the closure of the binding pocket by 16-19 degrees (Figure 3.10).

The flexibility of the apo (PDB ID: 8HTY) and holo (PDB ID: 5DN9) *Cb*FDH structures was compared by investigating the distribution of *B*-factor in each. In the apo structure, the thermal ellipsoids appear larger and in the spectrum from red to yellow to green (Figure 3.11-a). Conversely, in the holo structure, they are notably smaller and tend to be more spherical, primarily represented by dark blue (Figure 3.11-b).

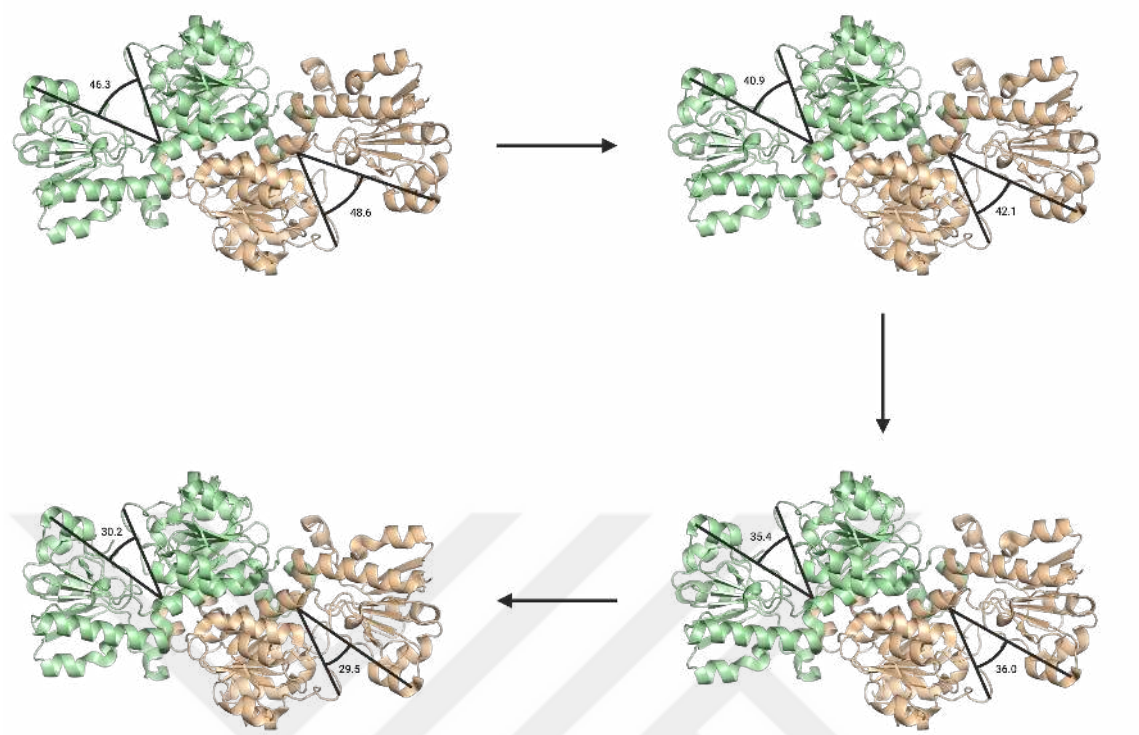

Figure 3.10: Closure of the binding pocket upon binding of NAD^+ and azide.

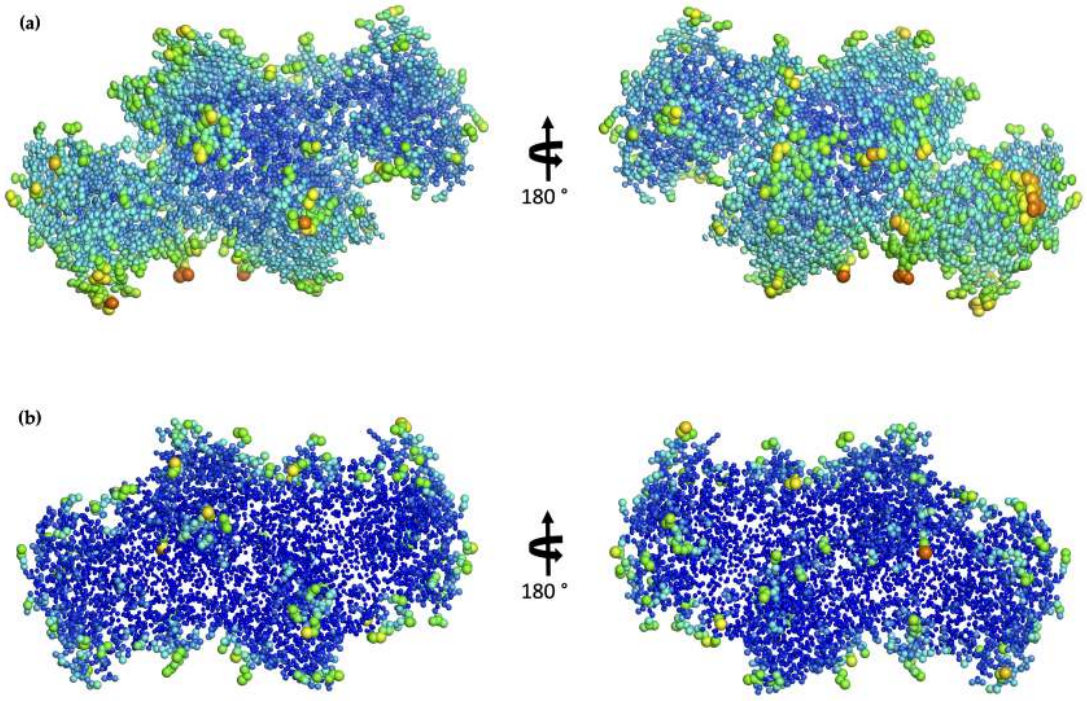

Figure 3.11: Thermal ellipsoid (*B*-factor distribution) representation of (a) apo and (b) holo wild-type *Cb*FDH structures.

3.3.3 Ambient Temperature Structure of Wild-type Apo CbFDH at 2.1 Å Resolution

The first ambient temperature crystal structure of wild-type apo *Cb*FDH was also determined at 2.1 Å resolution (PDB ID: 8IQ7). With an 85.9% overall completeness, the structure consists of two homodimers similar to the cryogenic structure (Figure 3.12). The Ramachandran statistics show that the favored and allowed regions contained 97.66% and 2.34% of the residues, respectively, with no outliers. Table 3.1 presents the statistics for data collection and refinement.

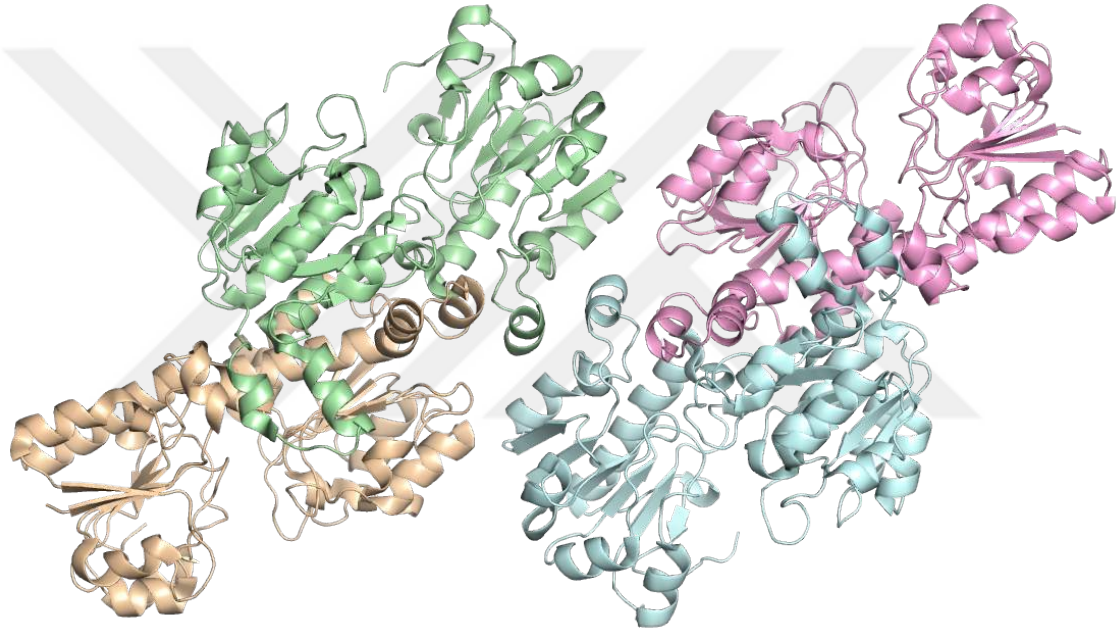

Figure 3.12: Wild-type apo *Cb*FDH structure at 2.1 Å resolution at ambient temperature.

3.3.4 Comparison of Cryogenic and Ambient Temperature Wild-type CbFDH Structures

Since the temperature may affect the conformation of protein molecules within a crystal, we superposed the *Cb*FDH structures determined at cryogenic and ambient temperature (Figure 3.13). The superposition gave an RMSD score of 0.55, suggesting that the two structures superposed with minor variations. The differences are mostly observed in the loop regions that are more flexible.

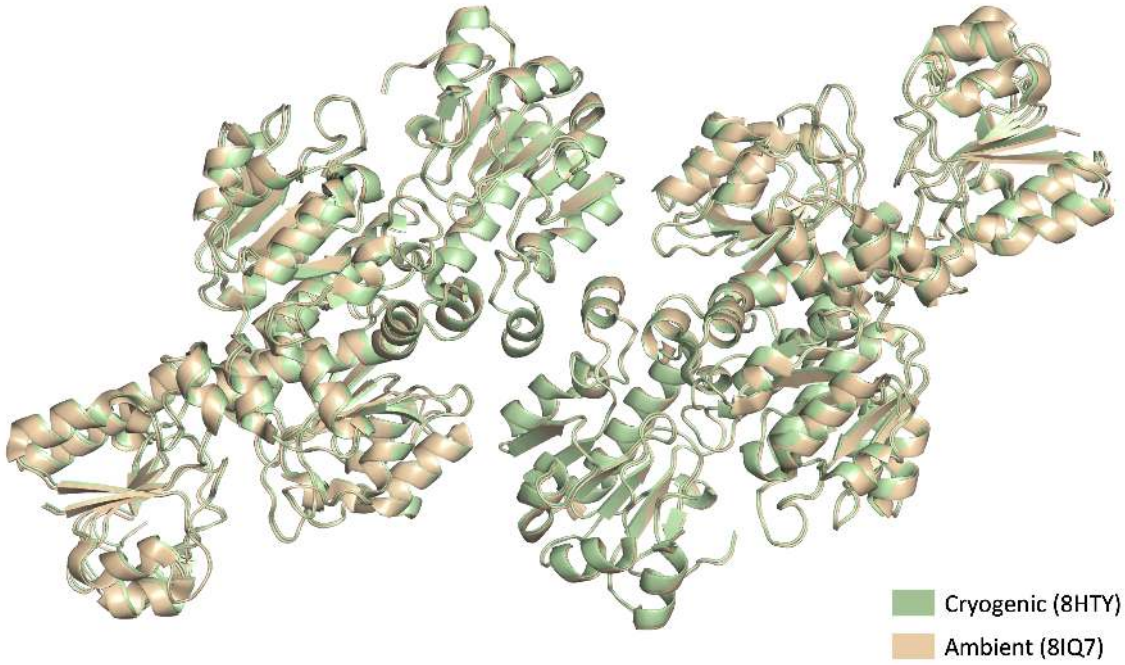

Figure 3.13: Superposition of cryogenic and ambient wild type *Cb*FDH structures.

In addition, we compared the cryogenic and ambient temperature wild-type structures by examining the number of water molecules determined in the electron density map. Our comparison revealed a significant difference between the two structures. While the cryogenic temperature structure had 2179 water molecules, the ambient temperature structure exhibited only 393 waters.

3.3.5 Cryogenic Temperature Structure of CbFDH Val120Thr Mutant

The crystal structure of the novel *Cb*FDH Val120Thr mutant was determined at 1.9 Å resolution at cryogenic temperature (PDB ID: 8IVJ). Similar to the wild type apo *Cb*FDH, this structure also consists of two homodimers. The overall completeness of the structure is 99.7%. The favored regions contain 98.02% of the residues while 1.98% are in the allowed regions with no outliers according to the Ramachandran plot. The data collection and refinement statistics are shown in Table 3.1.

An overall comparison between the wild type and Val120Thr mutant *Cb*FDH by superposition (RMSD: 0.27) showed that the single mutation does not impact the global protein structure significantly (Figure 3.14 and 3.15). Thus, the mutation site and its surroundings were visualized in more detail. We observed new hydrogen

bonds between Thr120 and three water molecules in the active site, which do not exist in the wild type *Cb*FDH (Figure 3.14 and 3.15).

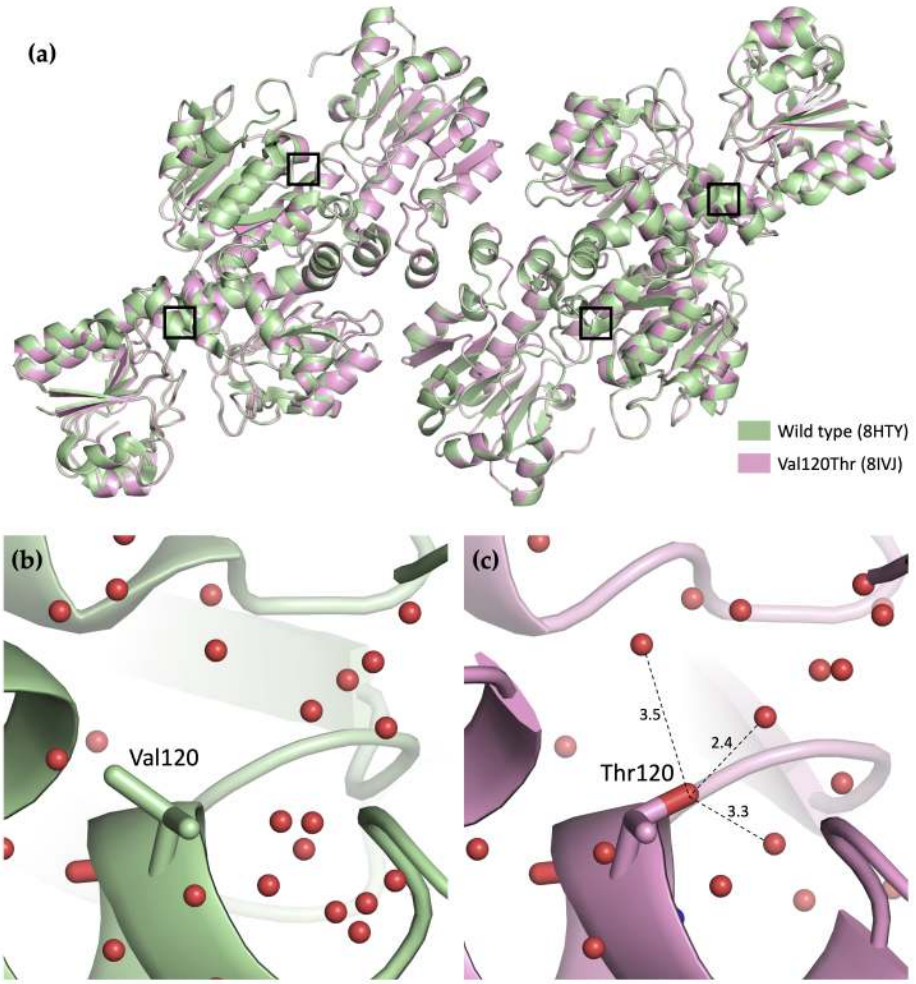

Figure 3.14: Comparison of wild type (PDB ID: 8HTY) and Val120Thr mutant (PDB ID: 8IVJ) *Cb*FDH. (a) Overall alignment of wild type and Val120Thr mutant *Cb*FDH. Wild-type is colored in pale green, Val120Thr in pink. (b) Val120 of the wild-type. (c) Thr120 of the Val120Thr mutant, demonstrating new hydrogen bonds formed between Thr120 and water molecules.

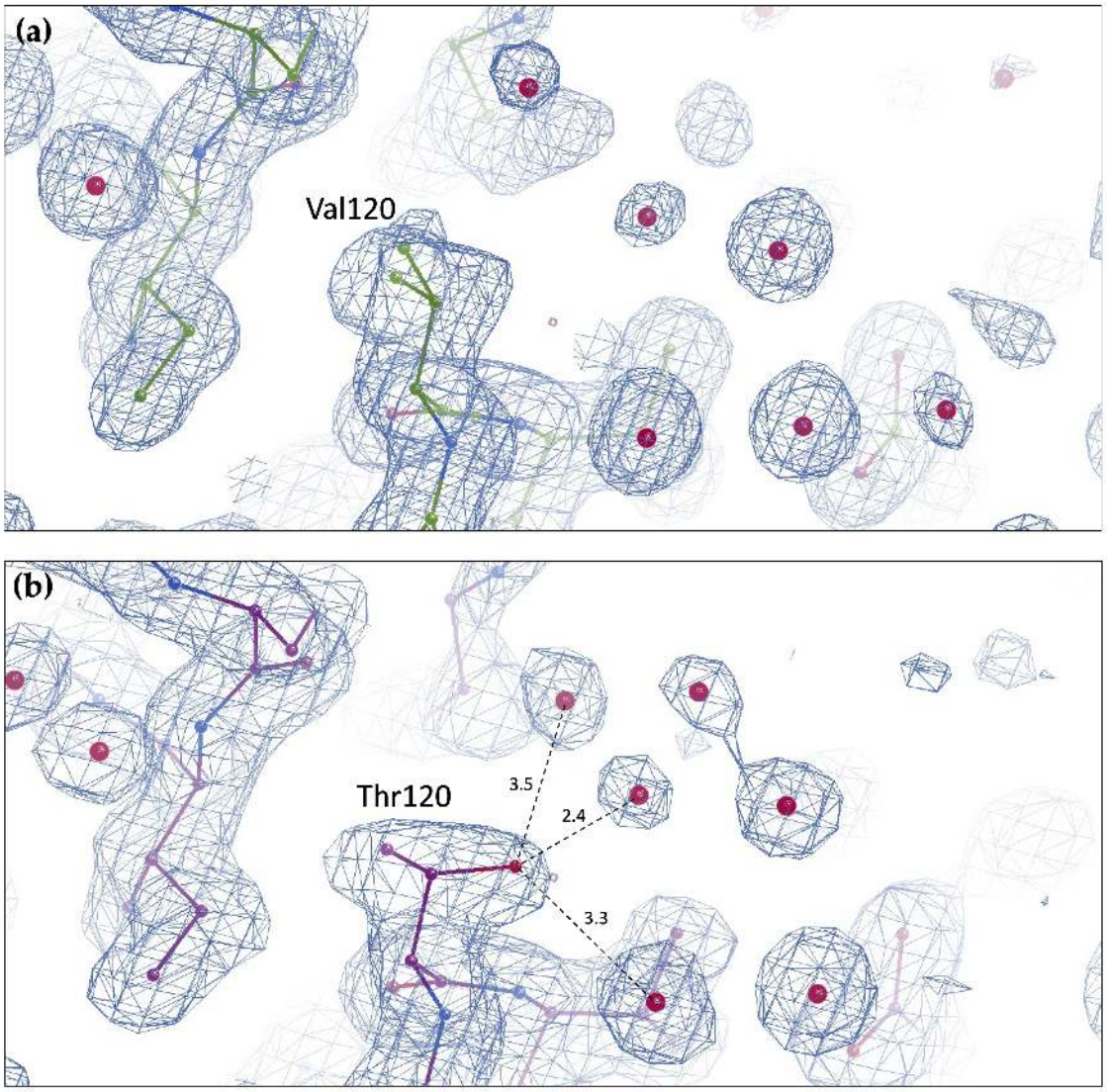

Figure 3.15: 2Fo-Fc simulated annealing-omit map of the 120$^{\text{th}}$ residue, colored in blue and contoured at 1.0 σ level. **(a)** Val120 of the wild type (8HTY). **(b)** Thr120 of the Val120Thr mutant (8IVJ). Hydrogen bond distances in Ångströms are shown with dashed lines.

Chapter 4

DISCUSSION AND CONCLUSION

The atomic-resolution wild-type apo *Cb*FDH structure determined (PDB ID: 8HTY) at cryogenic temperature reveals detailed structural features of the homodimeric enzyme. The electron density map, which is intact and visible even at high sigma levels, demonstrates the atomic details of the protein backbone, amino acid side chains, water molecules and other solution components like sulfate and MES. The structure determined consists of two homodimers of *Cb*FDH, which are found to have a high degree of similarity. Slight changes observed in the regions that are farther from the dimerization region are expected as they do not contribute to making contacts between the monomers and can move more freely.

Our cryogenic temperature apo wild-type *Cb*FDH structure was compared with a previously released apo wild type *Cb*FDH structure at 1.75 Å by superposition. The other structure also consists of two homodimers of the enzyme. The two structures aligned well, resulting in a small RMSD score. The minor differences between the two structures were mostly in the flexible loops and charged amino acid side chains that are directly exposed to the solvent. In addition, the electron density of our structure was better defined for the residues found in the more flexible regions of the protein.

In addition to comparison with the previous apo structure, the conformational shifts that take place upon binding of the coenzyme NAD^+ and the inhibitor azide were also investigated. Azide mimics the linear, triatomic structure of carbon dioxide, the substrate of the reverse reaction, therefore it can be used as an FDH inhibitor (Ohyama and Yamazaki, 1975). Upon alignment of the apo and holo *Cb*FDH structures, we observed conformational changes that span the whole structure, confirmed by high RMSD score of 1.80 Å. To understand the overall structural transformation as well as the movement of the binding pocket, morph analysis was performed

between the two states. The morph analysis revealed significant conformational alterations that lead to the closure of the binding cleft. This closure event prevents the entry of more coenzyme and substrate molecules into the active site. Moreover, the catalytic domain and binding domain come closer to a more compact configuration as a result of the global conformational change, making it favorable for the reaction.

Investigating protein structures at ambient temperature offers a deeper understanding into their conformational dynamics, functional processes, active site dynamicity, and how they interact with other molecules. Structures at ambient temperature can reveal a wider spectrum of structural variations, especially in proteins that are affected by extremely low temperatures (Fraser et al., 2011, Fischer, 2021). To gain a comprehensive understanding of protein structures and behavior, the first ambient temperature crystal structure of the apo wild-type *Cb*FDH was also determined. Superposition of the cryogenic and ambient temperature structures demonstrated that the temperature does not significantly affect the global structure of apo *Cb*FDH. The differences observed between the two structures are in the loop regions, which are expected to be more mobile than alpha-helices and beta-sheets. The reason for high similarity despite the great difference in temperature may be that the protein was frozen at a lower state of energy, which is similar to the state at ambient temperature. On the other hand, the main difference between these two structures is expected to be the mobility and flexibility of the protein at different temperatures. This can be investigated by comparing the *B*-factors; however, the resolution difference between the structures may have an impact on this comparison. Therefore, an ambient temperature structure at a higher resolution is required to understand the effect of temperature.

For further comparison between our cryogenic and ambient temperature wild-type *Cb*FDH structures, the number of water molecules identified within the two structures were also contrasted. 2179 water molecules defined within the cryogenic structure, compared to 393 in the ambient, demonstrates a great variance between the two structures. This significant variation in the number of identified water molecules between cryogenic and ambient temperatures sparks intriguing questions regarding the dynamic interplay between proteins and water under distinct environ-

mental conditions. The enhanced resolution attained at cryogenic temperatures greatly increases the precision of water molecule identification compared to the lower-resolution ambient temperature structures. Another factor contributing to the differences in identified water molecules may be the variances in water accessibility and occupancy between the two conditions. Cryogenic temperatures could potentially freeze water molecules within specific binding sites, thus stabilizing interactions that are transient at ambient temperatures (Nakasako, 2004). This phenomenon might elucidate why cryogenic temperature structures reveal a greater number of water molecules compared to ambient temperature structures. These observations highlights the necessity of considering temperature effects, as they introduce significant complexity to the protein's microenvironment, impacting conformational changes and water interactions due to environmental influences. Further investigations, such as molecular dynamics simulations and spectroscopic techniques, hold the potential to provide deeper insights into protein-water interactions and the behavior of water molecules.

The 120th residue within *Cb*FDH is a potential target for activity enhancement studies due to being located in the binding pocket where the substrate and coenzyme bind (Figure 1.5). For this reason, Val120 was mutated to threonine in our prior study. The reaction kinetics were assessed for the wild-type and Val120Thr mutant *Cb*FDH by measuring the absorbance during the reaction using a spectrophotometer (Bulut, 2019). The measurements were performed at 340 nm because NADH absorbs light at this wavelength while NAD^+ does not. The Michaelis-Menten and Lineweaver-Burk plots of the enzyme kinetics showed that the mutant enzyme has a lower K_M and a higher k_{cat} value. The lower K_M indicates that the substrate affinity of the mutant *Cb*FDH is higher compared to that of the wild-type enzyme. Additionally, the higher k_{cat} value indicates a faster conversion to the product. The k_{cat}/K_M value, also called catalytic efficiency, has been increased almost 10-fold in the mutant enzyme when compared to the wild-type. Since threonine is an amino acid that is more polar than valine, it may form hydrogen bonds with the solvent molecules and neighboring amino acids. These new bonds may lead to a higher stability in the substrate binding pocket. Furthermore, threonine's side chain is smaller

than valine's; therefore, it may provide a larger space for the substrate molecule to enter the substrate binding region.

The crystal structure of the Val120Thr mutant *Cb*FDH was determined at 1.9 Å resolution at cryogenic temperature to understand the effect of the mutation on the structure. Superposition of the cryogenic wild type and Val120Thr mutant *Cb*FDH revealed that the single mutation does not significantly impact the overall structure. Thus, a closer look at the mutation site and its surroundings is necessary. When the mutation site was investigated, new hydrogen bondings were observed between the mutated residue Thr120 and water molecules in the active site. The higher enzymatic activity measured in the mutant *Cb*FDH may be due to higher stability provided by these new hydrogen bonds in the active site. In addition, binding of the substrate or coenzyme molecules may be stabilized thanks to the new hydrogen bonds, contributing to a more efficient and rapid electron transfer. Also, threonine has an hydroxyl group in its side chain, which may be interacting with the coenzyme NAD^+ and other amino acids in the active site. Further experimental data is required, such as determining the structure of the Val120Thr mutant *Cb*FDH bound with the substrate/inhibitor and coenzyme, to fully understand the effect of the mutation.

The high-resolution structures of the apo *Cb*FDH provided in this study offer valuable insights into the enzyme's detailed structural characteristics. Furthermore, the incorporation of the Val120Thr mutation into the enzyme's active site resulted in a remarkable tenfold increase in enzymatic activity compared to the wild-type form. The discernible structural distinctions observed between the wild-type and mutant *Cb*FDH underscore the pivotal role of structural analysis in comprehending how mutations impact enzyme functionality. To gain a comprehensive understanding of the mutation's underlying mechanism, additional research involving the mutant enzyme in the presence of its substrate and coenzyme is imperative. Overall, the findings of this study hold potential to significantly contribute towards advancing enzymes with heightened efficiency and specificity, with broad implications spanning biotechnology, industry, and medicine.

BIBLIOGRAPHY

Adams, P. D., Afonine, P. V., Bunkóczi, G., Chen, V. B., Davis, I. W., Echols, N., Headd, J. J., Hung, L.-W., Kapral, G. J., Grosse-Kunstleve, R. W., McCoy, A. J., Moriarty, N. W., Oeffner, R., Read, R. J., Richardson, D. C., Richardson, J. S., Terwilliger, T. C., and Zwart, P. H. (2010). Phenix: a comprehensive python-based system for macromolecular structure solution. *Acta Crystallogr D Biol Crystallogr*, 66(Pt 2):213–221.

Aledo, J. C. and Medina, M. Á. (2019). Chapter 4 - thermodynamics of enzyme-catalyzed reactions. In Singh, R. S., Singhania, R. R., Pandey, A., and Larroche, C., editors, *Advances in Enzyme Technology*, Biomass, Biofuels, Biochemicals, pages 105–135. Elsevier.

Alissandratos, A., Kim, H.-K., and Easton, C. J. (2013). Formate production through biocatalysis. *Bioengineered*, 4(5):348–350. PMID: 23841981.

An, L. and Chen, R. (2016). Direct formate fuel cells: A review. *Journal of Power Sources*, 320:127–139.

Arnold, F. H. (1998). Design by directed evolution. *Accounts of Chemical Research*, 31(3):125–131.

Atalay, N., Akcan, E. K., Gul, M., Ayan, E., Destan, E., Kuzucu, F. B. E., Tokay, N., Cakilkaya, B., Nergiz, Z., Usta, G. K., Kepceoglu, A., Yapici, I., Tosun, B., Baldir, N., Yildirim, G., Johnson, J. A., Guven, O., Shafiei, A., Arslan, N. E., Yilmaz, M., Kulakman, C., Paydos, S. S., Cinal, Z. S., Sabanoglu, K., Pazarceviren, A., Yilmaz, A., Canbay, B., Asci, B., Kartal, E., Tavli, S., Caliseki, M., Gox, G., Mermer, A., Yesilay, G., Altuntas, S., Tateishi, H., Otsuka, M., Fujita, M., Tekin, S., Ciftci, H., Durdagi, S., Doganay, G. D., Karaca, E., Turkoz,

B. K., Kabasakal, B. V., Kati, A., and DeMirci, H. (2023). Cryogenic x-ray crystallographic studies of biomacromolecules at turkish light source "turkish delight". *Turkish Journal of Biology*, 47(1).

Balzer, G. J., Thakker, C., Bennett, G. N., and San, K.-Y. (2013). Metabolic engineering of escherichia coli to minimize byproduct formate and improving succinate productivity through increasing nadh availability by heterologous expression of nad(+)-dependent formate dehydrogenase. *Metab Eng*, 20:1–8.

Bar-Even, A. (2016). Formate assimilation: The metabolic architecture of natural and synthetic pathways. *Biochemistry*, 55(28):3851–3863.

Barin, R., Biria, D., Rashid-Nadimi, S., and Asadollahi, M. A. (2018). Enzymatic co2 reduction to formate by formate dehydrogenase from candida boidinii coupling with direct electrochemical regeneration of nadh. *Journal of CO2 Utilization*, 28:117–125.

Berríos-Rivera, S. J., Bennett, G. N., and San, K.-Y. (2002). Metabolic engineering of escherichia coli: increase of nadh availability by overexpressing an nad(+)-dependent formate dehydrogenase. *Metab Eng*, 4(3):217–229.

Braga Nan, L., Trably, E., Santa-Catalina, G., Bernet, N., Delgenès, J.-P., and Escudié, R. (2020). Biomethanation processes: new insights on the effect of a high h2 partial pressure on microbial communities. *Biotechnology for Biofuels*, 13(1):141.

Brannigan, J. A. and Wilkinson, A. J. (2002). Protein engineering 20 years on. *Nature Reviews Molecular Cell Biology*, 3(12):964–970.

Breen, L. T., Smyth, L. M., Yamboliev, I. A., and Mutafova-Yambolieva, V. N. (2006). beta-nad is a novel nucleotide released on stimulation of nerve terminals in human urinary bladder detrusor muscle. *Am J Physiol Renal Physiol*, 290(2):F486–95.

Brosnan, J. T. and Brosnan, M. E. (2020). Formate and its role in amino acid metabolism. *Current Opinion in Clinical Nutrition & Metabolic Care*, 23(1).

Bulut, H. (2019). *Production of NAD+-dependent formate dehydrogenase enzyme from Candida boidinii and enhancement of enzyme activity and thermal stability*. PhD thesis, Bezmialem Vakıf University.

Bulut, H., Yuksel, B., Gul, M., Eren, M., Karatas, E., Kara, N., Yilmazer, B., Kocyigit, A., Labrou, N. E., and Binay, B. (2021). Conserved amino acid residues that affect structural stability of candida boidinii formate dehydrogenase. *Applied Biochemistry and Biotechnology*, 193(2):363–376.

Calzadiaz-Ramirez, L. and Meyer, A. S. (2022). Formate dehydrogenases for co2 utilization. *Current Opinion in Biotechnology*, 73:95–100.

Carter, P. (1986). Site-directed mutagenesis. *Biochem J*, 237(1):1–7.

Carter, P. J. (2011). Introduction to current and future protein therapeutics: A protein engineering perspective. *Experimental Cell Research*, 317(9):1261–1269. Biotherapeutics.

Castillo, R., Oliva, M., Martí, S., and Moliner, V. (2008). A theoretical study of the catalytic mechanism of formate dehydrogenase. *The Journal of Physical Chemistry B*, 112(32):10012–10022.

Chayen, N. E. and Saridakis, E. (2008). Protein crystallization: from purified protein to diffraction-quality crystal. *Nature Methods*, 5(2):147–153.

Chica, R. A., Doucet, N., and Pelletier, J. N. (2005). Semi-rational approaches to engineering enzyme activity: combining the benefits of directed evolution and rational design. *Current Opinion in Biotechnology*, 16(4):378–384. Protein technologies and commercial enzymes.

Chirumamilla, R. R., Muralidhar, R., Marchant, R., and Nigam, P. (2001). Improving the quality of industrially important enzymes by directed evolution. *Molecular and Cellular Biochemistry*, 224(1):159–168.

Choe, H., Joo, J. C., Cho, D. H., Kim, M. H., Lee, S. H., Jung, K. D., and Kim, Y. H. (2014). Efficient co2-reducing activity of nad-dependent formate dehydrogenase from thiobacillus sp. knk65ma for formate production from co2 gas. *PLOS ONE*, 9(7):1–10.

Chueh, P.-J., Morré, D. M., and Morré, D. (2002). A site-directed mutagenesis analysis of tnox functional domains. *Biochimica et Biophysica Acta (BBA) - Protein Structure and Molecular Enzymology*, 1594(1):74–83.

Dasgupta, A., Chowdhury, N., and De, R. K. (2020). Metabolic pathway engineering: Perspectives and applications. *Computer Methods and Programs in Biomedicine*, 192:105436.

Dawson, R. (1986). *Data for Biochemical Research*. Oxford science publications. Clarendon Press.

Du, C., Li, Y., Xiang, R., and Yuan, W. (2022). Formate dehydrogenase improves the resistance to formic acid and acetic acid simultaneously in saccharomyces cerevisiae. *International Journal of Molecular Sciences*, 23(6).

Ducker, G. S. and Rabinowitz, J. D. (2017). One-carbon metabolism in health and disease. *Cell Metab*, 25(1):27–42.

Durnin, L., Dai, Y., Aiba, I., Shuttleworth, C. W., Yamboliev, I. A., and Mutafova-Yambolieva, V. N. (2012). Release, neuronal effects and removal of extracellular β-nicotinamide adenine dinucleotide (β-nad$^+$) in the rat brain. *Eur J Neurosci*, 35(3):423–435.

Emond, S. and Hollfelder, F. (2021). Triad: a transposition-based approach for

gene mutagenesis by random short in-frame insertions and deletions for directed protein evolution. *PROTOCOL*.

Emsley, P. and Cowtan, K. (2004). Coot: model-building tools for molecular graphics. *Acta Crystallogr D Biol Crystallogr*, 60(Pt 12 Pt 1):2126–2132.

Ertem, F. B., Guven, O., Buyukdag, C., Gocenler, O., Ayan, E., Yuksel, B., Gul, M., Usta, G., Cakılkaya, B., Johnson, J. A., Dao, E. H., Su, Z., Poitevin, F., Yoon, C. H., Kupitz, C., Hayes, B., Liang, M., Hunter, M. S., Batyuk, A., Sierra, R. G., Ketawala, G., Botha, S., Dağ, Ç., and DeMirci, H. (2022). Protocol for structure determination of sars-cov-2 main protease at near-physiological-temperature by serial femtosecond crystallography. *STAR Protocols*, 3(1):101158.

Fang, Z. and Chen, W. (2021). Recent advances in formic acid electro-oxidation: from the fundamental mechanism to electrocatalysts. *Nanoscale Adv.*, 3:94–105.

Fastrez, J. (2010). Engineering allosteric regulation into biological catalysts. *ChemInform*, 41(12).

Fauque, G. D. and Barton, L. L. (2012). Hemoproteins in dissimilatory sulfate- and sulfur-reducing prokaryotes. *Adv Microb Physiol*, 60:1–90.

Ferry, J. G. (1990). Formate dehydrogenase. *FEMS Microbiology Reviews*, 7(3-4):377–382.

Fischer, M. (2021). Macromolecular room temperature crystallography. *Quarterly Reviews of Biophysics*, 54:e1.

Fraser, J. S., van den Bedem, H., Samelson, A. J., Lang, P. T., Holton, J. M., Echols, N., and Alber, T. (2011). Accessing protein conformational ensembles using room-temperature x-ray crystallography. *Proceedings of the National Academy of Sciences*, 108(39):16247–16252.

Galkin, A. G., Kutsenko, A. S., Bajulina, N. P., Esipova, N. G., Lamzin, V. S., Mesentsev, A. V., Shelukho, D. V., Tikhonova, T. V., Tishkov, V. I., Ustinnikova, T. B., and Popov, V. O. (2002). Site-directed mutagenesis of the essential arginine of the formate dehydrogenase active centre. *Biochim Biophys Acta*, 1594(1):136–149.

Garman, E. F. and Owen, R. L. (2006). Cryocooling and radiation damage in macromolecular crystallography. *Acta Crystallographica Section D*, 62(1):32–47.

Gopalakrishnan, B., Khanna, N., and Das, D. (2019). Chapter 4 - dark-fermentative biohydrogen production. In Pandey, A., Mohan, S. V., Chang, J.-S., Hallenbeck, P. C., and Larroche, C., editors, *Biohydrogen (Second Edition)*, Biomass, Biofuels, Biochemicals, pages 79–122. Elsevier, second edition edition.

Griffiths, H. B., Williams, C., King, S. J., and Allison, S. J. (2020). Nicotinamide adenine dinucleotide (NAD+): essential redox metabolite, co-substrate and an anti-cancer and anti-ageing therapeutic target. *Biochemical Society Transactions*, 48(3):733–744.

Grubel, K., Jeong, H., Yoon, C. W., and Autrey, T. (2020). Challenges and opportunities for using formate to store, transport, and use hydrogen. *Journal of Energy Chemistry*, 41:216–224.

Gul, M., Ayan, E., Destan, E., Johnson, J. A., Shafiei, A., Kepceoglu, A., Yilmaz, M., Ertem, F. B., Yapici, I., Tosun, B., Baldir, N., Tokay, N., Nergiz, Z., Karakadioglu, G., Paydos, S. S., Kulakman, C., Ferah, C. K., Guven, O., Atalay, N., Akcan, E. K., Cetinok, H., Arslan, N. E., Sabanoglu, K., Asci, B., Tavli, S., Gumusboga, H., Altuntas, S., Otsuka, M., Fujita, M., Tekin, S., Çiftçi, H., Durdagi, S., Karaca, E., Kaplan Turkoz, B., Kabasakal, B. V., Kati, A., and DeMirci, H. (2023). Rapid and efficient ambient temperature x-ray crystal structure determination at turkish light source. *Scientific Reports*, 13(1):8123.

Guo, Q., Gakhar, L., Wickersham, K., Francis, K., Vardi-Kilshtain, A., Major, D. T., Cheatum, C. M., and Kohen, A. (2016). Structural and kinetic studies of formate dehydrogenase from candida boidinii. *Biochemistry*, 55(19):2760–2771.

Han, X., Wang, Q., Wu, Y., and Wu, C. (2022). Boosting formate production from co2 electroreduction over gas diffusion electrode with accessible carbon mesopores. *Electrochimica Acta*, 402:139526.

Hasan, M. M. (2023). Environment-friendly ascorbic acid fuel cell. *Electrochem*, 4(1):31–41.

Hovda, K. E., Lao, Y. E., Gadeholt, G., and Jacobsen, D. (2021). Formate test for bedside diagnosis of methanol poisoning. *Basic & Clinical Pharmacology & Toxicology*, 129(1):86–88.

Hu, L. and Adeyiga, A. A. (1997). Extraction of formic acid from sodium formate. *Industrial & Engineering Chemistry Research*, 36(6):2375–2379.

Jayathilake, B. S., Bhattacharya, S., Vaidehi, N., and Narayanan, S. R. (2019). Efficient and selective electrochemically driven enzyme-catalyzed reduction of carbon dioxide to formate using formate dehydrogenase and an artificial cofactor. *Accounts of Chemical Research*, 52(3):676–685.

Jiang, W., Lin, P., Yang, R., and Fang, B. (2016). Identification of catalysis, substrate, and coenzyme binding sites and improvement catalytic efficiency of formate dehydrogenase from candida boidinii. *Appl Microbiol Biotechnol*, 100(19):8425–8437.

Koch-Nolte, F., Fischer, S., Haag, F., and Ziegler, M. (2011). Compartmentation of nad+-dependent signalling. *FEBS Lett*, 585(11):1651–1656.

Kumar, S., Soni, R., and Kurungot, S. (2021). Pdp/wo3 multi-functional catalyst

with high activity and stability for direct liquid fuel cells (dlfcs). *Sustainable Energy Fuels*, 5:4758–4770.

Labrou, N. E. and Rigden, D. J. (2001). Active-site characterization of candida boidinii formate dehydrogenase. *Biochem J*, 354(Pt 2):455–463.

Lamarre, S. G., Morrow, G., Macmillan, L., Brosnan, M. E., and Brosnan, J. T. (2013). Formate: an essential metabolite, a biomarker, or more? *Clinical Chemistry and Laboratory Medicine*, 51(3):571–578.

Laskowski, R. A. and Swindells, M. B. (2011). Ligplot+: multiple ligand-protein interaction diagrams for drug discovery. *J Chem Inf Model*, 51(10):2778–2786.

Lehn, J.-M. and Ziessel, R. (1990). Photochemical reduction of carbon dioxide to formate catalyzed by 2,2t-bipyridine- or 1,10-phenanthroline-ruthenium(ii) complexes. *Journal of Organometallic Chemistry*, 382(1):157–173.

Lin, H. (2007). Nicotinamide adenine dinucleotide: beyond a redox coenzyme. *Org. Biomol. Chem.*, 5:2541–2554.

Lutz, S. (2010). Beyond directed evolution—semi-rational protein engineering and design. *Current Opinion in Biotechnology*, 21(6):734–743. Chemical biotechnology – Pharmaceutical biotechnology.

Lutz, S. and Iamurri, S. M. (2018). *Protein Engineering: Past, Present, and Future*, pages 1–12. Springer New York, New York, NY.

Maia, L. B., Moura, I., and Moura, J. J. G. (2021). *Carbon Dioxide Utilisation—The Formate Route*, pages 29–81. Springer International Publishing, Cham.

Martin-Amat, G., McMartin, K. E., Hayreh, S. S., Hayreh, M. S., and Tephly, T. R. (1978). Methanol poisoning: ocular toxicity produced by formate. *Toxicol Appl Pharmacol*, 45(1):201–208.

McCoy, A. J., Grosse-Kunstleve, R. W., Adams, P. D., Winn, M. D., Storoni, L. C., and Read, R. J. (2007). Phaser crystallographic software. *Journal of Applied Crystallography*, 40(4):658–674.

McPherson, A. (2017). *Protein Crystallization*, pages 17–50. Springer New York, New York, NY.

Miller, M., Robinson, W. E., Oliveira, A. R., Heidary, N., Kornienko, N., Warnan, J., Pereira, I. A. C., and Reisner, E. (2019). Interfacing formate dehydrogenase with metal oxides for the reversible electrocatalysis and solar-driven reduction of carbon dioxide. *Angewandte Chemie International Edition*, 58(14):4601–4605.

Mutafova-Yambolieva, V. N., Hwang, S. J., Hao, X., Chen, H., Zhu, M. X., Wood, J. D., Ward, S. M., and Sanders, K. M. (2007). Beta-nicotinamide adenine dinucleotide is an inhibitory neurotransmitter in visceral smooth muscle. *Proc Natl Acad Sci U S A*, 104(41):16359–16364.

Nakasako, M. (2004). Water-protein interactions from high-resolution protein crystallography. *Philos Trans R Soc Lond B Biol Sci*, 359(1448):1191–1204.

Nielsen, C. F., Lange, L., and Meyer, A. S. (2019). Classification and enzyme kinetics of formate dehydrogenases for biomanufacturing via co(2) utilization. *Biotechnol Adv*, 37(7):107408.

Niks, D. and Hille, R. (2018). Reductive activation of co(2) by formate dehydrogenases. *Methods Enzymol*, 613:277–295.

Nishi, K., Ueno, M., Murakami, Y., Fukunaga, N., Akuta, T., Kadowaki, D., Watanabe, H., Suenaga, A., Maruyama, T., and Otagiri, M. (2009). A site-directed mutagenesis study of drug-binding selectivity in genetic variants of human α1-acid glycoprotein. *Journal of Pharmaceutical Sciences*, 98(11):4316–4326.

Ohyama, T. and Yamazaki, I. (1975). Formate Dehydrogenase: Subunit and Mechanism of Inhibition by Cyanide and Azide. *The Journal of Biochemistry*, 77(4):845–852.

Ottone, C., Romero, O., Urrutia, P., Bernal, C., Illanes, A., and Wilson, L. (2021). *Enzyme Biocatalysis and Sustainability*, pages 383–413. Springer International Publishing, Cham.

Pietzke, M., Meiser, J., and Vazquez, A. (2020). Formate metabolism in health and disease. *Mol Metab*, 33:23–37.

Pinske, C. and Sawers, R. G. (2016). Anaerobic formate and hydrogen metabolism. *EcoSal Plus*, 7(1).

Punekar, N. S. (2018). *Regulation of Enzyme Activity*, pages 461–492. Springer Singapore, Singapore.

Reetz, M. T., Sun, Z., and Qu, G. (2023). *Introduction to Directed Evolution and Rational Design as Protein Engineering Techniques*, chapter 1, pages 1–28. John Wiley & Sons, Ltd.

Rojkova, A. M., Galkin, A. G., Kulakova, L. B., Serov, A. E., Savitsky, P. A., Fedorchuk, V. V., and Tishkov, V. I. (1999). Bacterial formate dehydrogenase. increasing the enzyme thermal stability by hydrophobization of alpha-helices. *FEBS Lett*, 445(1):183–188.

Sato, R. and Amao, Y. (2020). Can formate dehydrogenase from candida boidinii catalytically reduce carbon dioxide, bicarbonate, or carbonate to formate? *New J. Chem.*, 44:11922–11926.

Sawers, R. G., Blokesch, M., and Böck, A. (2004). Anaerobic formate and hydrogen metabolism. *EcoSal Plus*, 1(1).

Schrödinger, LLC (2015). The PyMOL molecular graphics system, version 1.8.

Siloto, R. M. and Weselake, R. J. (2012). Site saturation mutagenesis: Methods and applications in protein engineering. *Biocatalysis and Agricultural Biotechnology*, 1(3):181–189.

Slusarczyk, H., Felber, S., Kula, M. R., and Pohl, M. (2000). Stabilization of nad-dependent formate dehydrogenase from candida boidinii by site-directed mutagenesis of cysteine residues. *Eur J Biochem*, 267(5):1280–1289.

Song, J., Yang, Y., Yao, G., Zhong, H., He, R., Jin, B., Jing, Z., and Jin, F. (2017). Highly efficient synthesis of hydrogen storage material of formate from bicarbonate and water with general zn powder. *Industrial & Engineering Chemistry Research*, 56(22):6349–6357.

Tannous, C., Booz, G. W., Altara, R., Muhieddine, D. H., Mericskay, M., Refaat, M. M., and Zouein, F. A. (2021). Nicotinamide adenine dinucleotide: Biosynthesis, consumption and therapeutic role in cardiac diseases. *Acta Physiologica*, 231(3):e13551.

Tishkov, V. I., Galkin, A. G., Marchenko, G. N., Egorova, O. A., Sheluho, D. V., Kulakova, L. B., Dementieva, L. A., and Egorov, A. M. (1993). Catalytic properties and stability of a pseudomonas sp.101 formate dehydrogenase mutants containing cys-255-ser and cys-255-met replacements. *Biochem Biophys Res Commun*, 192(2):976–981.

Tishkov, V. I., Goncharenko, K. V., Alekseeva, A. A., Kleymenov, S. Y., and Savin, S. S. (2015). Role of a structurally equivalent phenylalanine residue in catalysis and thermal stability of formate dehydrogenases from different sources. *Biochemistry (Moscow)*, 80(13):1690–1700.

Tishkov, V. I., Matorin, A. D., Rojkova, A. M., Fedorchuk, V. V., Savitsky, P. A., Dementieva, L. A., Lamzin, V. S., Mezentzev, A. V., and Popov, V. O. (1996). Site-directed mutagenesis of the formate dehydrogenase active centre: role of the his332-gln313 pair in enzyme catalysis. *FEBS Letters*, 390(1):104–108.

Tishkov, V. I. and Popov, V. O. (2004). Catalytic mechanism and application of formate dehydrogenase. *Biochemistry (Moscow)*, 69(11):1252–1267.

Torres, R. A., Schiøtt, B., and Bruice, T. C. (1999). Molecular dynamics simulations of ground and transition states for the hydride transfer from formate to nad+ in the active site of formate dehydrogenase. *Journal of the American Chemical Society*, 121(36):8164–8173.

Vo, T., Purohit, K., Nguyen, C., Biggs, B., Mayoral, S., and Haan, J. L. (2015). Formate: an energy storage and transport bridge between carbon dioxide and a formate fuel cell in a single device. *ChemSusChem*, 8(22):3853–3858.

Wang, F., Cannon, A. T., Bhattacharya, M., Baumgarten, R., VanderLinden, R. T., and Saouma, C. T. (2020). Hydrogenation and electrocatalytic reduction of carbon dioxide to formate with a single co catalyst. *Chem. Commun.*, 56:12142–12145.

Wang, Y., Xue, P., Cao, M., Yu, T., Lane, S. T., and Zhao, H. (2021). Directed evolution: Methodologies and applications. *Chemical Reviews*, 121(20):12384–12444.

Weber, P. C. (1991). Physical principles of protein crystallization. In *Advances in Protein Chemistry*, volume 41, pages 1–36. Academic Press.

Yu, E. W., Aires, J. R., McDermott, G., and Nikaido, H. (2005). A periplasmic drug-binding site of the acrb multidrug efflux pump: a crystallographic and site-directed mutagenesis study. *Journal of Bacteriology*, 187(19):6804–6815.

Zeymer, C. and Hilvert, D. (2018). Directed evolution of protein catalysts. *Annual Review of Biochemistry*, 87(1):131–157. PMID: 29494241.

Zhang, X., Shao, W., Chen, B., and Wang, M. (2021). Cross-linking of carbonic anhydrase and formate dehydrogenase based on amino acid specific recogni-

tion: Conversion of carbon dioxide to formic acid. *Enzyme Microb Technol*, 146:109763.

Appendix A

CHEMICALS

Ampicillin	GOLDBIO
Chloramphenicol	GOLDBIO
Glycerol	ISOLAB
Imidazole	BioFroxx
IPTG	GOLDBIO
LB Agar	Caisson
NaCl	ISOLAB
HCl	ISOLAB
Ni-NTA	QIAGEN
Paraffin Oil	Tekkim Kimya
SDS	Sigma-Aldrich
Tris Base	Sigma-Aldrich
Triton X-100	Sigma-Aldrich
Tryptone	BD Biosciences
Yeast Extract	BD Biosciences

Appendix B

EQUIPMENT

ÄKTA go	Cytiva
Beckman Allegra 15R Centrifuge	Beckman Coulter
Beckman Avanti J-26S	Beckman Coulter
Beckman Optima™ L-80 XP Ultracentrifuge	Beckman Coulter
Beckman Ti-45 Rotor	Beckman Coulter
Branson W250 Sonifier	Branson
Cryovials	Wuxi NEST Biotechnology
Falcon Tubes	FIRATMED
Innova 44R	Eppendorf New Brunswick
Innova 4430R	Eppendorf New Brunswick
Kimtech Science KimWipes	Kimberly-Clark
NanoDrop™ 2000c	Thermo Scientific
Terasaki Plates	Greiner Bio-One
TGX-Mini Protean Gradient SDS-PAGE System	Bio-Rad Laboratories
Millipore Milli-Q Water Purification System	Merck Millipore
Oxford Cryosystems Cryostream 800 Plus	Oxford Cryosystems
Rigaku XtaLAB Synergy Flow XRD	Rigaku

Appendix C

PROTEIN LADDER

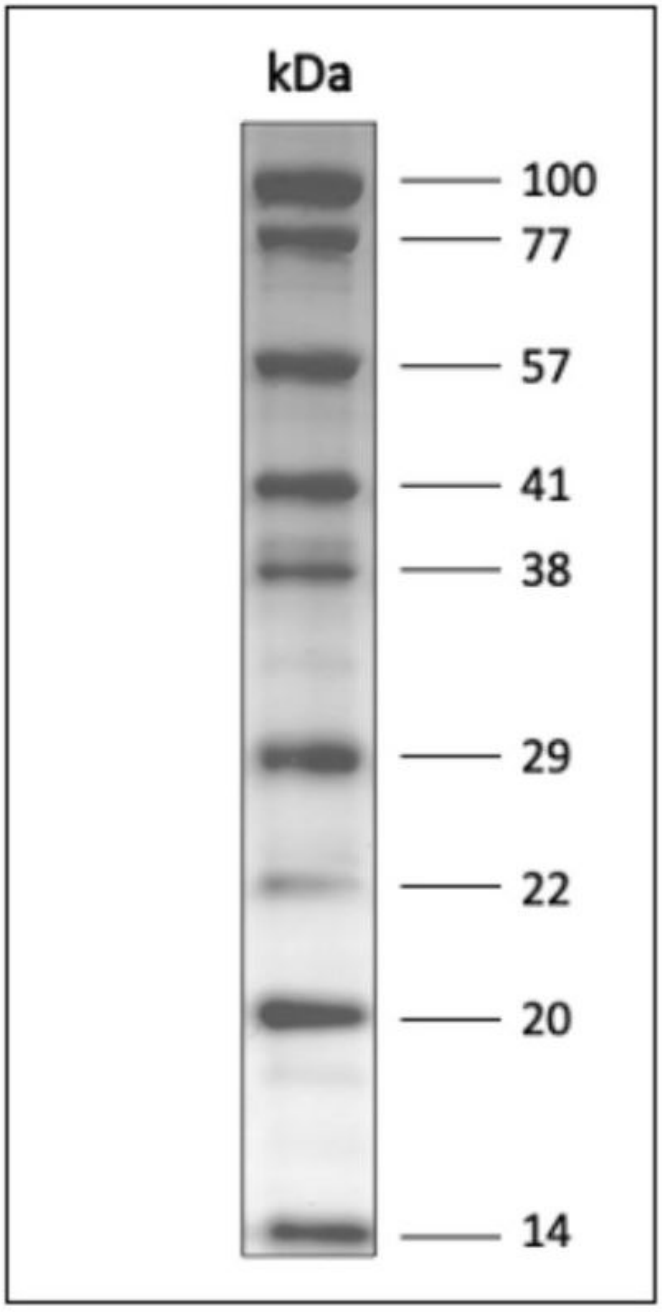

Figure C.1: KUYBIIGM Protein Ladder.

Appendix D

CRYSTALLIZATION SCREENS

3D Structure Screen	Molecular Dimensions
Clear Strategy Screen	Molecular Dimensions
Crystal Screen	Hampton Research
Crystal Screen Cryo	Hampton Research
Grid Screen Ammonium Sulfate	Hampton Research
Grid Screen MPD	Hampton Research
Grid Screen PEG/LiCl	Hampton Research
Grid Screen PEG6000	Hampton Research
Grid Screen Sodium Chloride	Hampton Research
Helix	Molecular Dimensions
Index	Hampton Research
Ionic Liquid Screen	Hampton Research
JBScreen Nuc-Pro	Jena Bioscience
JCSG	Molecular Dimensions
MacroSol	Molecular Dimensions
MembFac	Hampton Research
MIDAS	Molecular Dimensions
Morpheus	Molecular Dimensions
MultiXtal	Molecular Dimensions
Natrix	Hampton Research
NeXtal Protein Complex Suite	NeXtal Biotechnologies
NR-LBD	Molecular Dimensions
PACT Premier	Molecular Dimensions
PEG/Ion	Hampton Research
PEGRx	Hampton Research

PGA Screen	Molecular Dimensions
ProPlex Screen	Molecular Dimensions
Quik Screen	Hampton Research
SaltRx	Hampton Research
Structure Screen	Molecular Dimensions
Stura FootPrint Screen	Molecular Dimensions
Wizard	Rigaku
Wizard Cryo	Rigaku
Wizard Precipitant Synergy	Rigaku